

Simulating Raman spectra: A CP2K-based implementation and its application to defective graphene nanoribbons

Beat Hubmann

Supervised by Dr. Carlo A. Pignedoli

Co-supervised by Dr. Vasile Gradinaru

Swiss Federal Laboratories for Materials Science and Technology
ETH Zurich

August 2020

*A thesis submitted in partial fulfilment of the requirements for the degree of
Bachelor of Science ETH in Computational Science and Engineering.*

Abstract

During recent years, the laboratory nanotech@surfaces at Empa (Swiss Federal Laboratories for Materials Science and Technology) has successfully been fabricating increasingly complex atomically precise graphene nanoribbons (GNRs). An important aspect in the fabrication and characterization of carbon based nanomaterials such as GNRs is the comparison between measured and predicted spectroscopy and microscopy features key to the identification of so-called fingerprints of the fabricated nanostructures. Raman spectroscopy, which is based on a specific type of photon scattering, is a commonly used method to obtain such fingerprints. Currently, no straightforward out-of-the-box tool to predict Raman characteristics based on known molecular geometry exists.

My project uses the atomistic simulation software CP2K and Python-based numerical calculations based on density functional theory and the Placzek approximation to obtain Raman characteristics of a selection of graphene nanoribbons representative of the class of graphene nanoribbons fabricated by nanotech@surfaces at Empa. The goal of this endeavor is twofold: To estimate whether calculated Raman characteristics match experimental measurements for this particular class of systems, and to investigate whether the calculated Raman characteristics allow for the identification of and distinction between defects commonly occurring in the bottom-up fabrication of graphene nanoribbons as pioneered by nanotech@surfaces at Empa.

The obtained results indicate that while the calculated Raman characteristics come close to experimental observations, the match is not perfect. The chosen computational approach however seems very well suited to identifying and distinguishing fingerprints pertaining to common defects in graphene nanoribbons.

Contents

1	Introduction	1
1.1	Background to the Study	1
1.2	Aim, Scope, and Limitations	1
1.3	Overview of the Study	2
2	Graphene Nanoribbons	3
2.1	Introduction	3
2.2	Historical Perspective and Terminology	3
2.3	Properties and Synthesis of GNRs	5
2.4	Analysis and Characterization of GNRs	7
2.5	Computational Methods	8
2.6	Conclusion	8
3	Raman Spectroscopy	9
3.1	Introduction	9
3.2	Historical Perspective and Basics	10
3.3	Raman Spectroscopy Experiments	11
3.4	Raman Spectroscopy Computations	12
3.5	Comparing Experiment and Computation	16
3.6	Conclusion	17
4	Focus of Research	18
4.1	Introduction	18
4.2	Research Question	18
4.3	Sample Molecules	19

4.3.1	Verification Group with Reference Data	19
4.3.2	Small-to-medium GNRs Group with Experimental Data	20
4.3.3	Medium-to-large GNRs Group including Common Defects	20
5	Implementation of Computations	24
5.1	Introduction	24
5.2	Workflow Specification	24
5.3	Workflow Core Sections	26
5.3.1	Preparatory Steps	26
5.3.2	Quantum Chemical Calculations: CP2K	26
5.3.3	Computing Raman Spectra: Python with NumPy	26
6	Results	28
6.1	Introduction	28
6.2	Verification Group with Reference Data	28
6.2.1	Ethane	28
6.3	Small-to-medium GNRs Group with Experimental Data	29
6.3.1	7-AGNR (3 Units)	29
6.3.2	7-AGNR (6 Units)	30
6.4	Medium-to-large GNRs Group including Common Defects	34
6.4.1	7-AGNR (12 Units)	34
6.4.2	7-AGNR (12 Units): "Bite" Defect	35
6.4.3	7-AGNR (12 Units): Nitrogen Doping	36
6.4.4	7-AGNR (12 Units): Boron and Nitrogen Doping	37
7	Discussion	38
7.1	Introduction	38
7.2	Verification Group: Comparison with Reference Data	38
7.3	Small-to-medium GNRs Group: Comparison with Experimental Data	39
7.4	Medium-to-large GNRs Group: Distinction between Defects	41
7.5	Quantum Chemical Calculations with CP2K	42
7.6	Computing Raman Characteristics with Python and NumPy	42
8	Conclusion	43
References		44
Representative CP2K Configuration Files		49
Geometry Optimization Input File cp2k.inp		49

Vibrational Analysis Input File cp2k.inp	52
Python Source Code Key Excerpts	56
Computing the Raman Tensor from the Polarizability Tensor	56
Computing the Placzek Invariants	57
Computing Raman Intensities	58
Supplementary Results	59
Ethane	59
7-AGNR (3 units)	64
7-AGNR (6 units)	68
7-AGNR (12 units)	72
7-AGNR (12 units): "Bite" defect	76
7-AGNR (12 units): Nitrogen doping defect	80
7-AGNR (12 units): Nitrogen and boron doping defect	84
Declaration of Originality	88

List of Figures

2.1	GNRs with armchair (red), zigzag (black), and chiral (blue) edges, shown on graphene sheet (Talirz and Pignedoli, 2020).	5
2.2	Deposition of the molecular precursors (1) onto a crystalline noble metal surface at temperature $T = T_1$ activates their docking sites (2) by removing the halogen atoms. The activated radicals diffuse across the surface and polymerize (3). At elevated temperature $T_2 > T_1$, additional chemical bonds form (4), yielding the planar GNRs (Cai et al., 2010; Talirz and Pignedoli, 2020).	7
3.1	Schematic illustration of common scattering types. The upward arrows represent the excitation while downward arrows indicate the emission (Mitsutake et al., 2019).	11
3.2	Commonly adapted illumination-observation geometry: Incident radiation aligned with positive z axis, sample at coordinate origin, scattered radiation aligned with w vector (Long, 2002).	12
3.3	Setup of a typical Raman spectroscopy experiment (Deng et al., 2014).	16
3.4	Comparison of experimental and computed Raman spectra of BeO (Long, 2002).	17
4.1	Ethane molecule.	19
4.2	7-AGNR (3 units) molecule.	20
4.3	7-AGNR (6 units) molecule.	21
4.4	7-AGNR (12 units) molecule.	21
4.5	Defective 7-AGNR (12 units) molecule: "Bite" defect.	22
4.6	Defective 7-AGNR (12 units) molecule: Nitrogen doping.	22
4.7	Defective 7-AGNR (12 units) molecule: Nitrogen and boron doping.	23

5.1	Workflow for computing Raman characteristics.	25
6.1	Computed Ethane total Raman intensity.	29
6.2	Computed Ethane ($\lambda_L = 0\text{nm}$) total Raman cross-section.	29
6.3	Computed 7-AGNR (3 units) total Raman intensity.	30
6.4	Computed 7-AGNR (3 units) ($\lambda_L = 0\text{nm}$) total Raman cross-section.	30
6.5	Computed 7-AGNR (3 units) ($\lambda_L = 532\text{nm}$) total Raman cross-section.	31
6.6	Computed 7-AGNR (3 units) ($\lambda_L = 785\text{nm}$) total Raman cross-section.	31
6.7	Computed 7-AGNR (6 units) total Raman intensity.	32
6.8	Computed 7-AGNR (6 units) ($\lambda_L = 0\text{nm}$) total Raman cross-section.	32
6.9	Computed 7-AGNR (6 units) ($\lambda_L = 532\text{nm}$) total Raman cross-section.	33
6.10	Computed 7-AGNR (6 units) ($\lambda_L = 785\text{nm}$) total Raman cross-section.	33
6.11	Computed 7-AGNR (12 units) total Raman intensity.	34
6.12	Computed 7-AGNR (12 units) ($\lambda_L = 0\text{nm}$) total Raman cross-section.	34
6.13	Computed 7-AGNR (12 units) "bite" defect total Raman intensity.	35
6.14	Computed 7-AGNR (12 units) "bite" defect ($\lambda_L = 0\text{nm}$) total Raman cross-section.	35
6.15	Computed 7-AGNR (12 units) nitrogen doping total Raman intensity.	36
6.16	Computed 7-AGNR (12 units) nitrogen doping ($\lambda_L = 0\text{nm}$) total Raman cross-section.	36
6.17	Computed 7-AGNR (12 units) nitrogen and boron doping total Raman intensity.	37
6.18	Computed 7-AGNR (12 units) nitrogen and boron doping ($\lambda_L = 0\text{nm}$) total Raman cross-section.	37
7.1	Ethane: Comparison of experimental reference (Porezag and Pederson, 1996) and computed total Raman intensity.	39
7.2	7-AGNR (3 units): Comparison of experimental (Borin Barin, 2020) and computed total Raman intensity.	40
7.3	7-ANGR (12 units): Comparison of computed ($\lambda_L = 0\text{nm}$) total Raman cross-section for examined configurations.	41

List of Tables

3.1	Coefficients of linear combinations f, g of Placzek invariants.	15
7.1	Ethane reference total Raman intensities (Porezag and Pederson, 1996).	39

Introduction

1.1 | Background to the Study

During recent years, the laboratory nanotech@surfaces at Empa (Swiss Federal Laboratories for Materials Science and Technology) has successfully been fabricating increasingly complex atomically precise graphene nanoribbons (GNRs). Graphene nanoribbons are planar and finite graphene structures with a very high aspect ratio which are so narrow they are considered quasi-one-dimensional and are colloquially best described as strips of graphene. An important aspect in the fabrication and characterization of carbon based nanomaterials such as GNRs is the comparison between measured and predicted spectroscopy and microscopy features key to the identification of so-called fingerprints of the fabricated nanostructures. Raman spectroscopy, which is based on a specific type of photon scattering, is a commonly used method to obtain such fingerprints. Currently, no straightforward out-of-the-box tool to predict Raman characteristics based on known molecular geometry exists.

1.2 | Aim, Scope, and Limitations

The aim of this study is to establish the feasibility and usefulness of implementing an efficient procedure to simulate Raman characteristics of carbon-based nanomaterials using quantum chemical calculations and numerical methods based on the Placzek approximation.

To this end, the study covers the calculation of Raman characteristics for the following three sample groups (in increasing order of sample molecule complexity):

- A proof of concept for a non-graphene small organic molecule to verify the method.

- Analysis of two small-to-medium-sized defect-free GNRs for which experimental measurements are available.
- Analysis of a medium-to-large-sized GNR both defect-free and with three common GNR defect types.

In terms of limitations, no attempt to separate specific aspects of the simulated Raman characteristics into contributions from different molecular vibrational modes is made.

Also, no calculations beyond the Placzek approximation are attempted.

Finally, all calculations are made in simulated vacuum and without taking any substrate into account.

1.3 | Overview of the Study

The first two chapters following this introduction establish the necessary background knowledge and definitions.

Chapter 2 looks at graphene nanoribbons and their properties and characterizations relevant to this study. Chapter 3 serves to explain both the relevant theory of Raman scattering and the salient computational considerations. Based on chapters 2 and 3, chapter 4 details the specific sample molecules assigned to this study and highlights the research question. Chapter 5 illustrates the computational workflow as the method designed to answer the research question. The results of the computations are presented in chapter 6 and discussed in chapter 7. Finally, concluding remarks are given in chapter 8.

Graphene Nanoribbons

2.1 | Introduction

As laid out in the introduction, this study deals with the analysis and simulation of Raman characteristics as a way of fingerprinting graphene nanoribbons (GNRs).

To do so, the current chapter's aim is to establish the definition of graphene nanoribbons as a specific form of carbon based nanostructure and to set the scene for a more detailed explanation of the methods and techniques used later on.

To explain the peculiar physical properties of carbon nanostructures, analysis and characterization of their atomic structure is required. Due to the size scale, experimental analysis methods are not straightforward and often difficult to interpret. Computational methods are therefore useful to augment and extend experimental insights while being efficient in both cost and time.

After introducing and defining graphene nanoribbons, their most salient properties are listed. We then present an overview of current routes towards synthesizing graphene nanoribbons and finish with a look at both experimental and computational characterization methods.

2.2 | Historical Perspective and Terminology

Graphene nanoribbons (GNRs) are a specific type of graphene, a crystalline carbon allotrope in the form of a single-layered hexagonal lattice with carbon atoms at each vertex. Graphene per se has a rich potential of possible applications in engineering and science (Geim and Novoselov, 2007). GNRs in specific have started to attract increased research interest (Fujita et al., 1996) about a decade after the discovery of fullerene

molecules (Kroto et al., 1985) invigorated interest in nanoscale carbon structures. Initially used mainly as a convenient theoretical model in the 1990s (Fujita et al., 1996; Klein, 1994; Nakada et al., 1996), a decade later experiments demonstrated the semiconducting properties of GNRs (Novoselov et al., 2004), paving the way towards possible applications in digital electronics. The descriptive term *ribbon* in GNRs stems from the fact that GNRs are not infinite two-dimensional like a graphene layer, but instead are strips of graphene finite both in length and width with an aspect ratio such that they effectively can be considered one-dimensional systems. According to present day conventions, GNRs are generally less than 100nm wide and often are fabricated to measure only between 5nm and 50nm wide (Nakada et al., 1996; Talirz and Pignedoli, 2020).

A deciding characteristic of GNRs is their peripheral shape or edge structure. This shape stems directly from the direction along which a raw sheet of graphene would have to be cut to obtain the ribbon under consideration. The two possible higher-order structures topologically mandated by the characteristics of the one-layer graphene carbon lattice are designated *armchair* and *zigzag* (Fujita et al., 1996). Figure 2.1 shows sample ribbons of the armchair (AGNR, red) and the zigzag (ZGNR, black) type. Here, blue marks *chiral* ribbons, a third designation given to those ribbons which originate from cutting a graphene sheet in an intermediate direction (Talirz and Pignedoli, 2020).

The width of ANGRs is given as N_A , the number of carbon dimers across the ribbon at the wider sections including the edges. Consequently, the width of ZGNRs is given as N_Z , the number of zigzag lines formed by the carbon atoms when viewed along the ribbons, also including the edges (see figure 2.1 for both). There is no further commonly accepted terminology for GNRs. Especially notable is the absence of any naming convention for decorating the carbon atoms sitting at the edges with other chemical species. Where not stated otherwise, it is standard practice to implicitly assume open bond deactivation by hydrogen atoms.

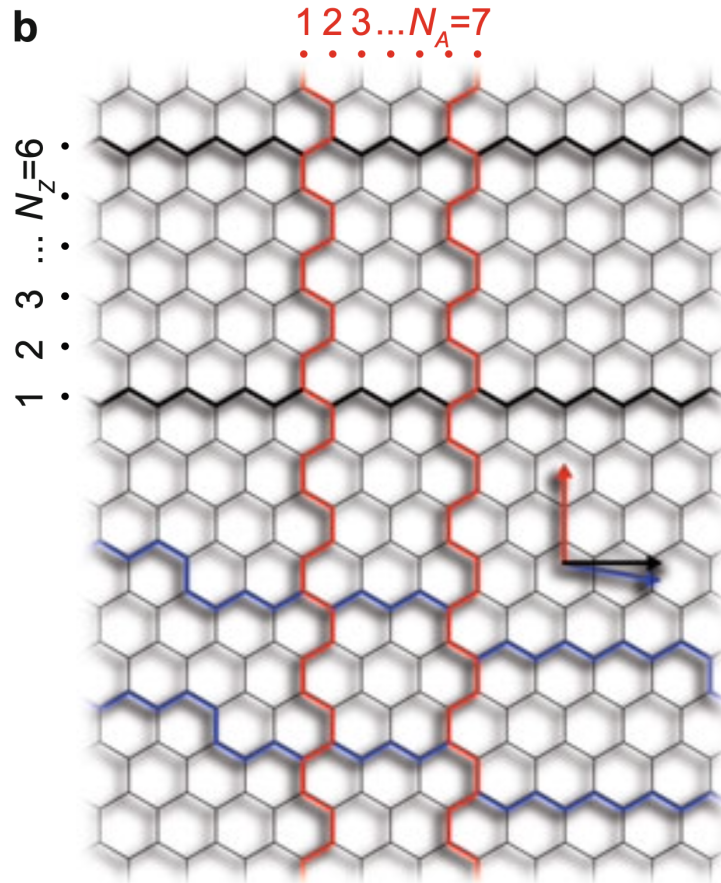


Figure 2.1: GNRs with armchair (red), zigzag (black), and chiral (blue) edges, shown on graphene sheet (Talirz and Pignedoli, 2020).

2.3 | Properties and Synthesis of GNRs

In general, all physical properties of GNRs strongly depend on their edge structure as introduced above as well as on their atomic precision or structural perfection. Structural perfection in this context signifies absence of any defects in terms of conformation or doping purity. While the majority of current interest in GNRs is rooted in their electronic properties as already hinted at above, their mechanical and optical properties also warrant interest. At the nanometer scale, direct testing of deformation under mechanical strain currently is out of experimental reach, but simulation methods predict an extremely high Young's modulus (Bu et al., 2009). Again, mechanical properties seem to depend on the specific geometry of GNR samples. The optical properties of GNRs again differ depending on geometry as manifested in different selection rules for opti-

cal transitions (Lin and Shyu, 2000).

Graphene in itself has attracted enormous attention for electronic applications (Cheng et al., 2012), but its lack of a bandgap limits its potential for general purpose transistors (Schwierz, 2013). However, cutting graphene into GNRs offers a way to create a bandgap via quantum confinement while maintaining graphene's other positive electronic properties (Barone et al., 2006; Talirz and Pignedoli, 2020). Rule-of-thumb calculations show that the minimum bandgap of 0.4 eV required for a transistor on/off ratio in the $10^4 - 10^6$ range as required for digital logic circuits (Kim et al., 2011) can only be obtained by making AGNRs no more than a few nanometers equivalent to about 50 carbon atoms wide (Berger et al., 2006).

Naturally, fabricating structures of such small dimensions and thus highly sensitive to irregularities in their edge structure and purity for the use in experiments or demonstrator devices is a daunting task. The different routes towards the production of GNRs explored in recent years can be sorted into several major groups: Chemical vapor deposition was first to be implemented (Murayama and Maeda, 1990) and followed by what could be summarized as chemical (Affoune et al., 2001), lithographic (Chen et al., 2007), unzipping (Cano-Márquez et al., 2009), and bottom-up synthesis (Cai et al., 2010) methods.

The most precise and thus most promising results to date have been obtained by a bottom-up approach combining two of the earlier techniques: Molecular precursors designed to obtain a desired electronic structure as determined by GNR width, edge structure, and edge passivation are synthesized in solution. These precursors are then evaporated onto a crystalline noble metal surface. With their docking sites such activated, the precursors diffuse and polymerize onto the noble metal surface. After additional carbon bond formation is achieved at an elevated temperature, the formed GNRs then ideally uniformly conform to the electronic properties brought about by their design geometry (see figure 2.2).

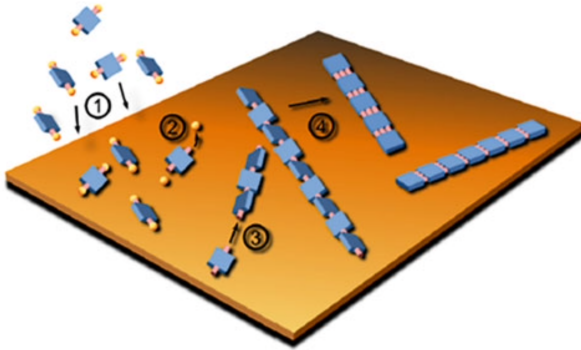


Figure 2.2: Deposition of the molecular precursors (1) onto a crystalline noble metal surface at temperature $T = T_1$ activates their docking sites (2) by removing the halogen atoms. The activated radicals diffuse across the surface and polymerize (3). At elevated temperature $T_2 > T_1$, additional chemical bonds form (4), yielding the planar GNRs (Cai et al., 2010; Talirz and Pignedoli, 2020).

2.4 | Analysis and Characterization of GNRs

Common to all forms of GNRs no matter what the synthesis method or the exact geometry is the requirement for analysis and characterization. The reasons are twofold: Firstly, defects are very much relevant for the properties of nanostructures and thus need to be discovered and quantified; and secondly, only the study especially of the electronic structure of GNRs allows predictions on their mechanical, optical and electronic properties. The characterization techniques employed in the analysis of GNRs on substrates so far belong into two major groups: Spectroscopy methods such as Raman spectroscopy (Malard et al., 2009) and infrared spectroscopy (Sasaki et al., 2018) as well as scanning probe microscopy methods such as scanning tunneling microscopy (Lahiri et al., 2010). While scanning probe microscopy methods offer precise imaging of the atomic structure as well as characterization of the electronic properties, they are elaborate in terms of equipment and procedures and are generally only applied to small samples. Raman and infrared spectroscopy on the other hand are well suited to the quick analysis of larger samples with regard to the presence of defects and geometric properties such as average GNR length. Infrared spectroscopy being a fairly recent technique in this context, Raman spectroscopy is currently considered the most ideal method for the characterization of GNR samples on a substrate (Overbeck et al., 2019).

2.5 | Computational Methods

To complement and verify GNR data obtained by the experimental characterization methods described above, computational methods are employed to calculate GNR properties based on their molecular structure. These methods mostly revolve around either microscopic, that is quantum mechanical, calculations using density functional theory (Baroni et al., 2001) but also include classical macroscopic molecular dynamics (Neek-Amal and Peeters, 2010) and, for the investigation of the mechanical rather than electronic properties of GNRs, even finite element methods (Georgantzinos et al., 2011).

In broad terms, the aim of these computational methods is to first establish a sample molecule's total energy in relation to the molecule's specific geometric and electronic configuration. Then, depending on the quantity of interest, the changes in the molecule's total energy when subjected to change-of-energy-inducing stimulation of an electronic or mechanical nature are quantified.

2.6 | Conclusion

Having established GNRs as a structure of interest with several interesting properties, we are now well aware of the necessity of analysis and characterization. Raman spectroscopy as a well established method is best suited to analyzing the most recent bottom-up synthetization methods as developed by nanotech@surfaces at Empa. Also, Raman spectroscopy is ideally complemented by computational methods to verify and predict experimental measurements.

Raman Spectroscopy

3.1 | Introduction

As Raman spectroscopy currently is the accepted method of choice for characterizing materials of the GNR class (Overbeck et al., 2019), its experimental aspects need to be understood. As it is desirable especially for reasons of cost and efficiency to be able to compute Raman characteristics in addition to experimental measurements, the computation of Raman characteristics is just as relevant.

The current chapter looks at the experimental setup and corresponding geometrical aspects of Raman spectroscopy measurements and then mirrors those considerations from a computational perspective. This is complemented by a sample comparison between experimentally measured and computed Raman characteristics.

After a short historical review and a minimum amount of definitions, we take a look at the geometry and coordinate system as well as the parameters of a common experimental setup. Moving on to the computational aspects, computation of the Raman tensor including the rotational invariants derived from said tensor is introduced. Finally, a chain of simplifications leads to an expression enabling the comprehensive comparison of different sample molecules with regards to their Raman scattering behavior.

3.2 | Historical Perspective and Basics

Scattering of light with change of frequency was discovered by C. V. Raman in 1928 (Raman and Krishnan, 1928) when examining the scattering of focused light in vapors and liquids. Raman's discovery followed the preceding theory on scattering of light without change of frequency, also called elastic scattering, as formulated by Rayleigh in 1871. Consequently, as it involves a change of frequency, Raman scattering is often called inelastic scattering (see figure 3.1 for both). Further theoretical predictions on Raman scattering processes were made soon after Raman's discovery, for example by Placzek (Placzek, 1934), but the fact that spontaneous Raman scattering is several orders of magnitude less common than Rayleigh scattering made experimental measurements difficult. Only the availability of working laser devices several decades later allowed extended experiments involving large numbers of finely frequency-tuned photons. In Raman spectroscopy, incident monochromatic photons generated by a laser and thus with a precisely tuned frequency interact with the sample matter's structure: Described conceptually, the incoming photon gets annihilated, resulting in two effects: A perturbation-induced transition of the sample molecule to a different energy state and the creation and scattering of a new photon with a different frequency. First considering the effect on the sample molecule, the change of energy state translates into a change of molecular vibrational energy realized by the sample molecule switching to a different vibrational mode. Using a quantum mechanical approach, vibrations of the molecular lattice can be quantized. A quantum of vibration is called a phonon, a virtual particle, with the total vibrational energy of a molecule being equal to the sum of all individual phonons' energies. Considering on the other hand the newly created scattered photon, conservation of energy dictates that this photon ends up with a frequency matching the change of energy of the sample molecule it originates from. Overall, there are two principal cases: If the energy of the sample molecule is increased during the process and the molecule is excited to a higher vibrational mode, the scattered photon carries a lower frequency, corresponding to a lower energy, than the incident photon. Such a shift in frequency is called a Stokes shift in analogy to Stokes' law statement on the frequency of fluorescent light when compared to the excitation frequency. Conversely, if the sample molecule ends up in a lower vibrational energy state, this comes with an increase in frequency, and thus energy, of the scattered photon with regard to the incident photon and is called an Anti-Stokes shift. Taken together and their intensity recorded all over the spectrum, these Raman shifts in frequency of scattered incoming phonons constitute a Raman spectrum. The Raman spectrum can thus serve as a fingerprint of the molecu-

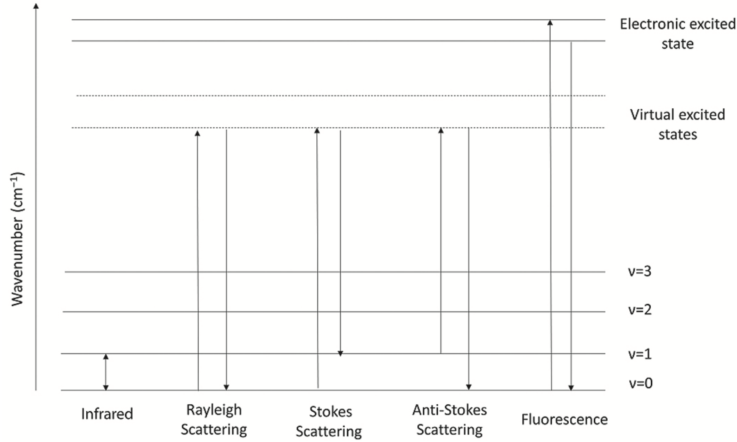


Figure 3.1: Schematic illustration of common scattering types. The upward arrows represent the excitation while downward arrows indicate the emission (Mitsutake et al., 2019).

lar structure of a material sample system as manifested by its vibrational modes, which makes the Raman spectrum well suited to identifying sample constituents and defects.

3.3 | Raman Spectroscopy Experiments

When considering actual experimental setups for Raman spectroscopy, the geometry describing incident illumination and scattering observation needs to be defined. While in principle any laboratory or fixed in space coordinate reference system can be used, it is most convenient and acceptable without loss of generality to choose a coordinate system simplifying most geometrical expressions. The commonly adapted choice thus is a space-fixed right-handed cartesian coordinate system in which the sample material is placed at the origin. The positive z axis is aligned with the incident photon radiation, while the $x - z$ plane is aligned with the scattered photons traveling along an observation vector w at an observation angle θ from the positive z axis (see figure 3.2). Commonly used observation angles are $\theta = 0$ for forward scattering, $\theta = \frac{\pi}{2}$ for 90° scattering and $\theta = \pi$ for retro (or back) scattering, all of them further simplifying geometrical considerations. The incident radiation is typically set to be polarized with the electric vector parallel to the y axis and thus perpendicular to the $x - z$ scatter plane. It is a simplifying idealization that also the scattered photons form a narrow beam fixed in diameter just like the incident laser radiation instead of radiating in all directions, but experimental setups can be arranged to closely approximate this assumptions. Further-

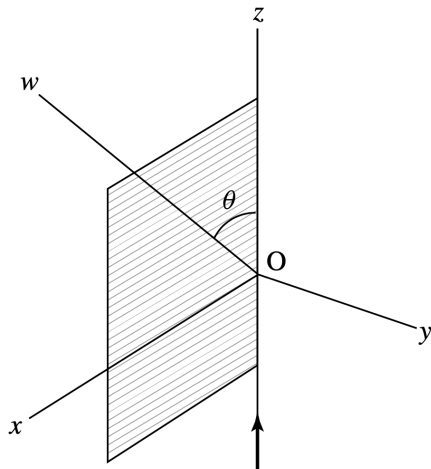


Figure 3.2: Commonly adapted illumination-observation geometry: Incident radiation aligned with positive z axis, sample at coordinate origin, scattered radiation aligned with w vector (Long, 2002).

more, it can be shown (Long, 2002) that for this experimental setup, deviating from this ideal assumption of the scattered beam does not change the calculated intensities of the scattered radiation when considering isotropic scattering.

Also, the specific choice of coordinate system ends up having no influence on the final Raman intensities: Considering the isotropic average over all possible orientations in space of the sample molecules makes intensity expression agnostic of the choice of coordinate system. The remaining experimental parameters are the frequency ω_L and hence the wavelength λ_L of the incident laser radiation as well as the temperature T at which the experiment is conducted. The laser wavelengths most widely used in experiment are 532nm, 785nm and 1064nm. A temperature of 300K is generally adopted for Raman spectroscopy experiments.

3.4 | Raman Spectroscopy Computations

The first step towards calculating Raman spectra based on the known or assumed structure of a molecule is the relaxation of the molecule conformation into a minimum energy state through geometry optimization.

Having done that, there are several routes to obtaining the vibrational normal modes of the molecule which are required for calculating Raman spectra. In the simplest case, the potential energy surface is assumed to behave like a harmonic potential around the

energetic minimum. The vibrational frequencies are then directly deduced from the second derivatives of the potential energy with regard to individual atomic displacements. A more sophisticated approach to obtain Raman spectra which considers anharmonic effects and is especially suitable for solvation or bulk model samples is ab initio molecular dynamics (AIMD) (Luber et al., 2014; Thomas et al., 2013). Finally, a most generic approach to obtain lattice properties is ab initio quantum mechanical calculations using density functional (perturbation) theory (Baroni et al., 2001; Porezag and Pederson, 1996).

Following the basic approach laid out by the above established methods (Porezag and Pederson, 1996), we first calculate the sample molecule's vibrational eigenmodes in the harmonic approximation based on the potential energy surface obtained by density functional theory. Having obtained the molecule's vibrational normal modes and, as a function of the molecular vibrational frequencies, polarizability tensor ϵ , the Raman tensor α can be calculated (Liang et al., 2019; Porezag and Pederson, 1996) as given in equation 3.1.

$$\alpha_{i\beta\gamma} = \frac{\sqrt{\Omega}}{4\pi} \sum_{ni\gamma} \frac{\partial \epsilon_{\beta\gamma}}{\partial u_{inv}} e_{in\gamma} \frac{1}{\sqrt{m_n}} \quad (3.1)$$

Here, $\frac{\partial \epsilon_{\beta\gamma}}{\partial u_{inv}}$ is obtained as the finite difference derivative of the polarizability tensor $\epsilon_{\beta\gamma}$ with respect to an atom-specific displacement u_{inv} along the direction ν for normal mode i and atom n . The corresponding eigenvector of the dynamical matrix is given by $e_{in\gamma}$, while m_n is the mass of the respective atom. Finally, β and γ are placeholders for the spatial coordinates x, y, z .

Having obtained the Raman tensor, the three Placzek rotation invariants (Placzek, 1934) are formed: $G_{i,0}$ (equation 3.2) represents the mean polarizability of mode i while $G_{i,1}$ (equation 3.3) stands for the respective antisymmetric anisotropy and $G_{i,2}$ (equation 3.4) represents the corresponding anisotropy. In literature, these rotation invariants are more commonly but interchangeably expressed as $a_i^2 = \frac{1}{3}G_{i,0}$, $\delta_i^2 = \frac{3}{2}G_{i,1}$ and $\gamma_i^2 = \frac{3}{2}G_{i,2}$.

$$G_{i,0} = \frac{1}{3}(\alpha_{ixx} + \alpha_{iyy} + \alpha_{izz})^2 \quad (3.2)$$

$$G_{i,1} = \frac{1}{2}[(\alpha_{ixy} - \alpha_{iyx})^2 + (\alpha_{ixz} - \alpha_{izx})^2 + (\alpha_{izy} - \alpha_{iyz})^2] \quad (3.3)$$

$$G_{i,2} = \frac{1}{2}[(\alpha_{ixy} + \alpha_{iyx})^2 + (\alpha_{ixz} + \alpha_{izx})^2 + (\alpha_{izy} + \alpha_{iyz})^2] \\ + \frac{1}{3}[(\alpha_{ixx} - \alpha_{iyy})^2 + (\alpha_{ixx} - \alpha_{izz})^2 + (\alpha_{izz} - \alpha_{iyy})^2] \quad (3.4)$$

Evidently, for a symmetric Raman tensor $G_{i,1}$ reduces to $G_{i,1} = 0$ while $G_{i,2}$ simplifies to $G_{i,2} = 2[\alpha_{ixy}^2 + \alpha_{iyz}^2 + \alpha_{izx}^2] + \frac{1}{3}[(\alpha_{ixx} - \alpha_{iyy})^2 + (\alpha_{ixx} - \alpha_{izz})^2 + (\alpha_{izz} - \alpha_{iyy})^2]$.

For all observation angles $\theta \in \{0, \frac{\pi}{2}, \pi\}$ commonly used in experiment and linearly polarized incident radiation with the electric vector perpendicular to the $x - z$ plane as described above and hereafter designated \perp^{inci} , a modular closed expression for the intensity I of the scattered radiation for any given sample molecule vibrational mode can be derived (equation 3.5; Long (2002)). Herein, the polarization state of the scattered radiation is considered for the states perpendicular $p^s = \perp^s$ and parallel $p^s = \parallel^s$ to the scatter plane. Furthermore, we have $k_{\tilde{v}} = \pi^2 / \epsilon_0^2$ and N_{v^i} as the number of sample molecules in the initial vibrational state v^i . The wavenumber of the scattered radiation is given by $\tilde{v}_s = \tilde{v}_{\text{inci}} \pm |\tilde{v}_{vf v^i}|$ wherein \tilde{v}_{inci} is the wavenumber of the incident radiation with $\tilde{v}_{\text{inci}} = \tilde{v}_L$ for the common experimental setup with an illuminating laser. The magnitude of the wavenumber associated with the (Anti-)Stokes vibrational transition of the sample molecule from v^i to v^f is given by $|\tilde{v}_{vf v^i}|$. Most importantly, f and g respectively are linear combinations of the rotation invariants a, δ, γ and G_0, G_1, G_2 respectively (see table 3.1 for the coefficients of the linear combinations). The rotation invariants in turn are functions of the hyperparameter observation angle θ . Finally, $\mathcal{I} = \frac{1}{2}c_0\epsilon_0 E_y^2$ is the irradiance of the incident radiation.

$$\begin{aligned} I(\theta; p^s, \perp^{\text{inci}}) &= k_{\tilde{v}} N_{v^i} \tilde{v}_s^4 \left[\frac{1}{45} f(a^2, \gamma^2, \delta^2; \theta) \right] \mathcal{I} \\ &= k_{\tilde{v}} N_{v^i} \tilde{v}_s^4 \left[\frac{1}{30} g(G_0, G_1, G_2; \theta) \right] \mathcal{I} \end{aligned} \quad (3.5)$$

Using several steps, additional expressions for the differential scattering cross-sections σ' of the two polarizations can be obtained for each sample molecule vibrational mode i with frequency ω_i . These expressions represent the rate at which energy is removed from the incident beam (Weber and Merlin, 2011) and are not only simpler to handle, but by being independent of irradiance of the incident radiation also facilitate comparing the scattering intensity fingerprints of different sample molecules: Starting from the expression for intensity I , we recognize from table 3.1 containing the respective coefficients for the Placzek invariants that the intensity I is identical for all observation angles $\theta \in \{0, \frac{\pi}{2}, \pi\}$. Doing away with constant factors by division, inserting the Bose occupation factor $n(v_i) + 1 = (1 - \exp \frac{-hc\tilde{v}_i}{k_B T})^{-1}$ standing in for N_{v^i} as the number of sample molecules, and finally using the relationship between intensity and irradiance $\sigma' = \frac{d\sigma}{d\Omega} = \frac{I}{\mathcal{I}}$, we arrive at the desired expressions (equations 3.6 and 3.7) for the considered experimental setup. The only remaining parameters now are \tilde{v}_L for the laser wavenumber and T for the system temperature.

	$f(\cdot)$			$g(\cdot)$		
	a^2	δ^2	γ^2	G_0	G_1	G_2
$\theta = 0$						
\perp^s	45	0	4	10	0	4
\parallel^s	0	5	3	0	5	3
$\theta = \frac{\pi}{2}$						
\perp^s	45	0	4	10	0	4
\parallel^s	0	5	3	0	5	3
$\theta = \pi$						
\perp^s	45	0	4	10	0	4
\parallel^s	0	5	3	0	5	3

Table 3.1: Coefficients of linear combinations f, g of Placzek invariants.

$$\begin{aligned} \sigma'_i(\perp^s) &\sim \frac{1}{1 - \exp \frac{-hc\tilde{\nu}_i}{k_B T}} \frac{(\tilde{\nu}_L - \tilde{\nu}_i)^4}{\tilde{\nu}_i} \frac{45a_i^2 + 4\gamma_i^2}{45} \\ &\sim \frac{1}{1 - \exp \frac{-hc\tilde{\nu}_i}{k_B T}} \frac{(\tilde{\nu}_L - \tilde{\nu}_i)^4}{\tilde{\nu}_i} \frac{10G_{i,0} + 4G_{i,2}}{30} \end{aligned} \quad (3.6)$$

$$\begin{aligned} \sigma'_i(\parallel^s) &\sim \frac{1}{1 - \exp \frac{-hc\tilde{\nu}_i}{k_B T}} \frac{(\tilde{\nu}_L - \tilde{\nu}_i)^4}{\tilde{\nu}_i} \frac{5\delta_i^2 + 3\gamma_i^2}{45} \\ &\sim \frac{1}{1 - \exp \frac{-hc\tilde{\nu}_i}{k_B T}} \frac{(\tilde{\nu}_L - \tilde{\nu}_i)^4}{\tilde{\nu}_i} \frac{5G_{i,1} + 3G_{i,2}}{30} \end{aligned} \quad (3.7)$$

The final desired expression for the omnidirectional scattering cross-section best suited for averaging over all possible sample molecule orientations (equation 3.8) is obtained by adding $\sigma'_i(\perp^s)$ and $\sigma'_i(\parallel^s)$ from equations 3.6 and 3.7.

$$\begin{aligned} \sigma'_i(\perp^s + \parallel^s) &\sim \frac{1}{1 - \exp \frac{-hc\tilde{\nu}_i}{k_B T}} \frac{(\tilde{\nu}_L - \tilde{\nu}_i)^4}{\tilde{\nu}_i} \frac{45a_i^2 + 5\delta_i^2 + 7\gamma_i^2}{45} \\ &\sim \frac{1}{1 - \exp \frac{-hc\tilde{\nu}_i}{k_B T}} \frac{(\tilde{\nu}_L - \tilde{\nu}_i)^4}{\tilde{\nu}_i} \frac{10G_{i,0} + 5G_{i,1} + 7G_{i,2}}{30} \end{aligned} \quad (3.8)$$

3.5 | Comparing Experiment and Computation

Figure 3.3 details a standard setup of a Raman experiment to measure intensities of scattered radiation with both parallel and perpendicular polarization.

Having obtained the vibrational modes' omnidirectional scattering cross-sections as derived above resulting in equation 3.8, we set the obtained maximum differential scattering cross-section over all vibrational modes i to an arbitrary fixed value. All other modes' cross-section values are scaled accordingly to facilitate comparison between different sample molecules and experiments. Finally, figure 3.4 shows a representative result of a basic sample comparison between experiment and computation for the Raman spectrum of Bromellite (BeO).

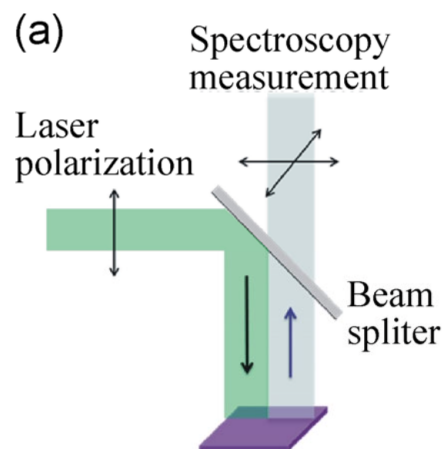


Figure 3.3: Setup of a typical Raman spectroscopy experiment (Deng et al., 2014).

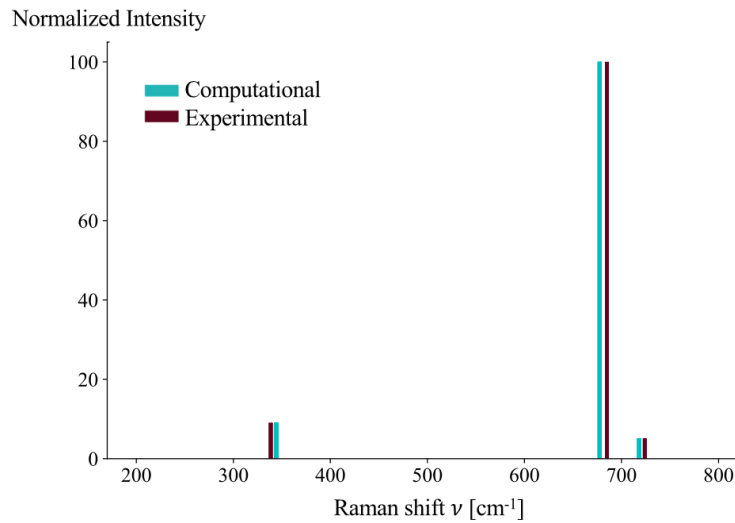


Figure 3.4: Comparison of experimental and computed Raman spectra of BeO (Long, 2002).

3.6 | Conclusion

Having established knowledge about the setup, geometry and parameters of Raman scattering experiments and having gone through the computational steps to obtain a normalized Raman spectrum for a given sample molecule, all necessary parts for conducting the computations assigned to this report are in place.

Focus of Research

4.1 | Introduction

As shown so far, experimental and computational Raman spectroscopy is well suited to characterizing molecules. While widely applied to simple crystals (Ceriotti et al., 2006; Liang et al., 2019) and minerals (Lafuente et al., 2015), steps towards characterizing larger molecules have also been undertaken (Neugebauer et al., 2002; Reiher et al., 2003). It therefore is an obvious choice to use the introduced method to compute Raman spectra of GNR molecules representative of those synthesized by nanotech@surfaces at Empa and compare the spectra with each other and with experimental measurements where available.

To this end, we define a selection of test sample molecules.

4.2 | Research Question

The introduced method is used to calculate the Raman spectrum of three groups of sample molecules: A verification group consisting of a simple organic compound, a group of small-to-medium GNRs free of defects for which experimental spectra are available, and finally a group of medium-to-large GNRs with a focus on common defects which occur naturally or by design during synthetization by the bottom-up approach as pioneered by nanotech@surfaces at Empa (Pizzochero et al., 2020).

For the first and the second group where reference or experimental data are available, actual and computed Raman characteristics are plotted enabling direct comparison and assessment of the degree of similarity.

For the third group, calculated Raman characteristics are compared between the defect-free sample and the samples with disorders with the aim of identifying fingerprints characteristic to the defects.

4.3 | Sample Molecules

4.3.1 | Verification Group with Reference Data

4.3.1.1 | Ethane

Ethane (figure 4.1) is a hydrocarbon molecule with the chemical formula C_2H_6 with a total count of 8 atoms and 7 bonds and a molecular mass of 30.069 g/mol. At standard pressure and temperature as encountered during the reference spectroscopy experiment, it is a colorless gas.

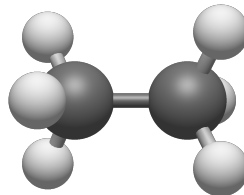


Figure 4.1: Ethane molecule.

4.3.2 | Small-to-medium GNRs Group with Experimental Data

4.3.2.1 | Defect-free GNR: 7-AGNR (3 Units)

7-AGNR (3 units) (figure 4.2) is a GNR molecule whose edge structure is in armchair configuration. It has the chemical formula $C_{42}H_{20}$ with a total count of 62 atoms and 74 bonds and a molecular mass of 524.619 g/mol. It consists of three connected anthracene units.

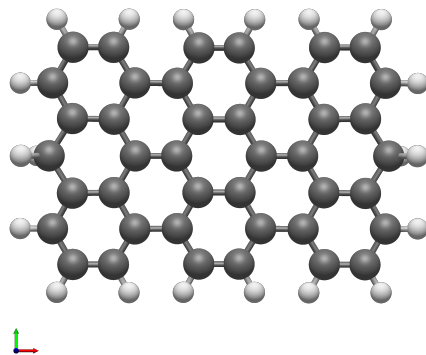


Figure 4.2: 7-AGNR (3 units) molecule.

4.3.2.2 | Defect-free GNR: 7-AGNR (6 Units)

7-AGNR (6 units) (figure 4.3) is a GNR molecule whose edge structure is in armchair configuration. It has the chemical formula $C_{84}H_{32}$ with a total count of 116 atoms and 143 bonds and a molecular mass of 1041.175 g/mol. It consists of six connected anthracene units.

4.3.3 | Medium-to-large GNRs Group including Common Defects

4.3.3.1 | Defect-free GNR: 7-AGNR (12 Units)

7-AGNR (12 units) (figure 4.4) is a GNR molecule whose edge structure is in armchair configuration. It has the chemical formula $C_{168}H_{56}$ with a total count of 224 atoms and 281 bonds and a molecular mass of 2074.287 g/mol. It consists of twelve connected anthracene units.

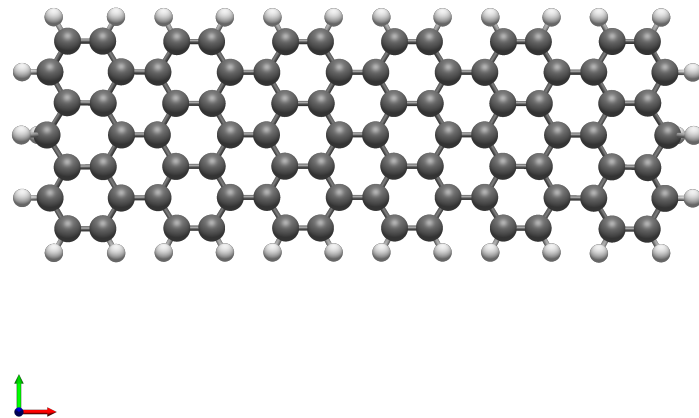


Figure 4.3: 7-AGNR (6 units) molecule.

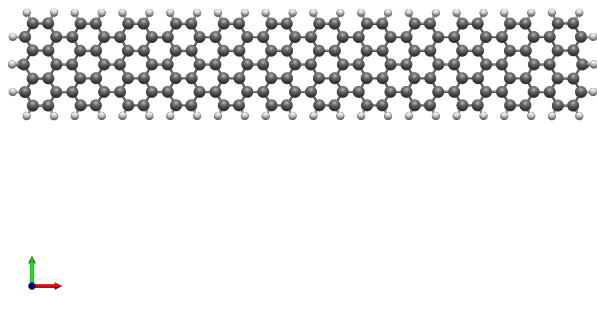


Figure 4.4: 7-AGNR (12 units) molecule.

4.3.3.2 | Defective GNR: 7-AGNR (12 Units): "Bite" Defect

This is the 7-AGNR (12 units) molecule as presented in subsection 4.3.3.1 above, but with a bite-shaped defect in the form of a benzene ring having two carbon atoms removed near the middle of the molecule (figure 4.5). It has the chemical formula $C_{166}H_{56}$ with a total count of 222 atoms and 278 bonds and a molecular mass of 2050.265 g/mol.

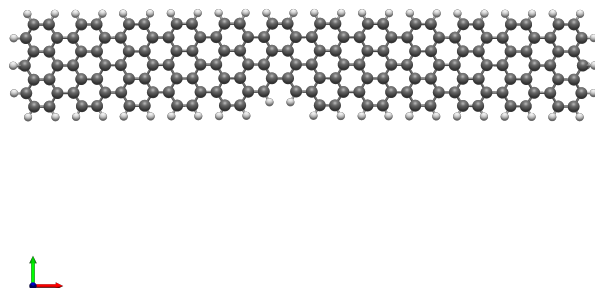


Figure 4.5: Defective 7-AGNR (12 units) molecule: "Bite" defect.

4.3.3.3 | Defective GNR: 7-AGNR (12 Units): Nitrogen Doping

This is the 7-AGNR (12 units) molecule as presented in subsection 4.3.3.1 above, but with two carbon atoms replaced by nitrogen atoms in a single benzene ring near the middle of the molecule (figure 4.6). It has the chemical formula $C_{166}H_{56}N_2$ with a total count of 224 atoms and 281 bonds and a molecular mass of 2078.277 g/mol.

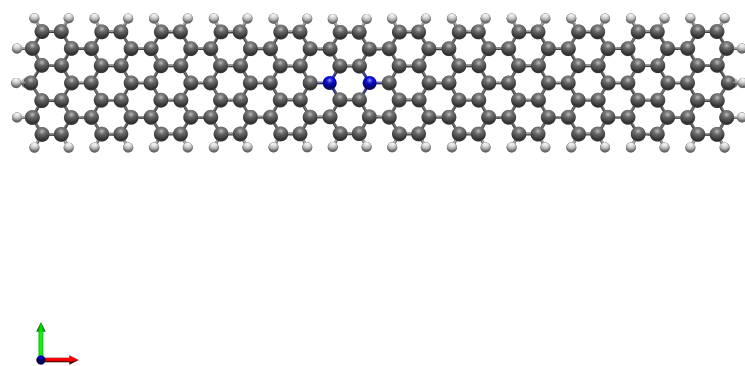


Figure 4.6: Defective 7-AGNR (12 units) molecule: Nitrogen doping.

4.3.3.4 | Defective GNR: 7-AGNR (12 Units): Boron and Nitrogen Doping

This is the 7-AGNR (12 units) molecule as presented in subsection 4.3.3.1 above, but with a single benzene ring near the middle of the molecule replaced by a single borazine ring (figure 4.7). It has the chemical formula $C_{162}H_{56}B_3N_3$ with a total count of 224 atoms and 281 bonds and a molecular mass of 2076.657 g/mol.

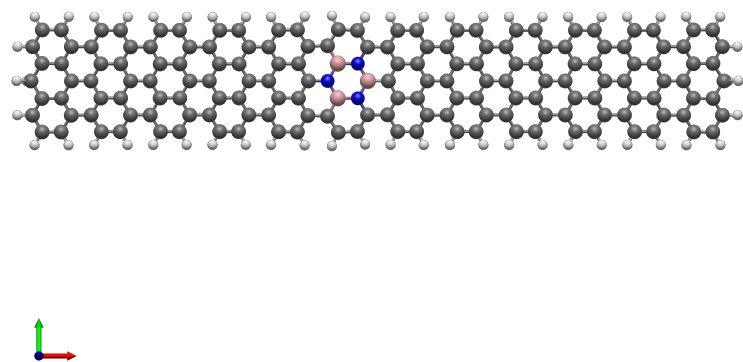


Figure 4.7: Defective 7-AGNR (12 units) molecule: Nitrogen and boron doping.

Implementation of Computations

5.1 | Introduction

This chapter details the computational workflow which is dominated by two components: First, quantum chemical calculations are performed using the atomistic simulation software CP2K (Hutter et al., 2014). In turn, Raman calculations based on intermediate results are performed by a Python/NumPy code. Code files for all workflow steps are openly accessible (Hubmann, 2020).

5.2 | Workflow Specification

The two main computational components of the workflow as mentioned above are bookended by the preparatory steps and the plotting of the obtained Raman spectra. Figure 5.1 depicts the complete workflow.

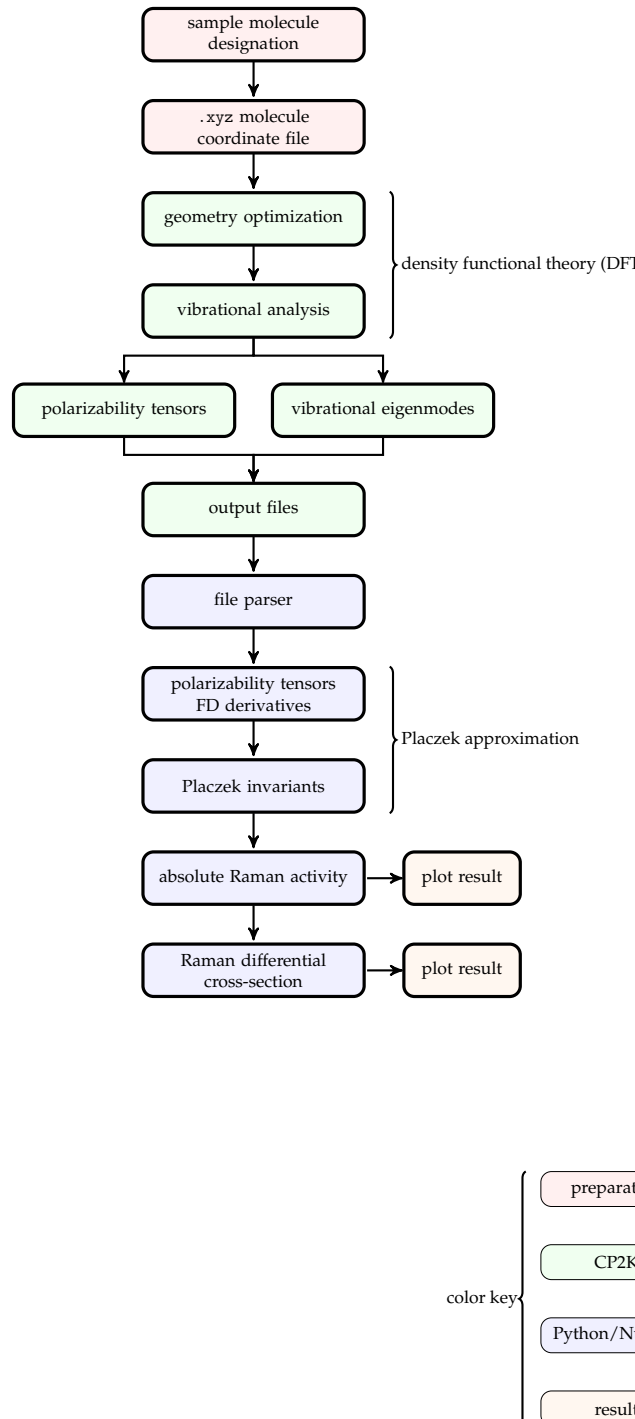


Figure 5.1: Workflow for computing Raman characteristics.

5.3 | Workflow Core Sections

5.3.1 | Preparatory Steps

First, the chosen sample molecule's geometry is written into a .xyz (XYZ) cartesian coordinate file on a per-atom basis, preferably using the atomic simulation environment (ASE) library (Hjorth Larsen et al., 2017) for Python or alternatively a semantic chemical editor such as Avogadro (Hanwell et al., 2012).

5.3.2 | Quantum Chemical Calculations: CP2K

CP2K (Hutter et al., 2014) is an open-source atomistic simulation tool in the field of density functional theory (DFT) and beyond-DFT approaches. It is highly versatile with respect to the computational methods and the combinations thereof to solve a given problem. Its capability to describe the dynamics of large systems with hundreds of atoms render it very well suited to the study of GNRs and their properties. Out of CP2K's many functionalities, this study uses DFT based forces to first optimize atomic positions within the sample molecules towards an energetic minimum and then to perform a full vibrational analysis of the samples based on finite differences:

The .xyz coordinate file is read into CP2K to perform a geometry optimization to relax the molecule into energetically optimal conformation.

After calculating the optimized atomic coordinates, the resulting coordinate file serves as the basis for the DFT based vibrational analysis.

The CP2K input configuration files for a typical geometry optimization and vibrational analysis are given in appendix A.

5.3.3 | Computing Raman Spectra: Python with NumPy

Following the vibrational analysis step, a Python program reads the optimized molecule geometry together with all CP2K output files and parses their content into NumPy (van der Walt et al., 2011) data structures.

The Python program then calculates the polarizability tensor first derivatives with regard to cartesian coordinates using a central finite differences 3-point scheme. From this, the mass weighted polarizability tensor first derivatives with regard to normal coordinates of the vibrational modes are calculated.

With the key elements of the Raman tensor for each vibrational mode now computed, the Placzek invariants for mean polarizability, anisotropy and asymmetric anisotropy

are computed. Based on the three Placzek invariants, the parameter-independent absolute Raman intensity for the commonly implemented experimental setup is calculated.

Finally, the Raman cross-section depending on incident radiation source frequency and experimental system temperature is computed from the absolute Raman activity and plotted for further analysis.

Results

6.1 | Introduction

This chapter presents the computed absolute total Raman intensities $I(\perp^s + \parallel^s, \perp^{\text{inci}})$ as well as the computed Raman total cross-sections $\sigma'_i(\perp^s + \parallel^s; \tilde{\nu}_L, T)$ over the full spectrum of vibrational modes computed by CP2K for all three groups of sample molecules.

The system temperature is set at $T = 300\text{K}$ for all calculations.

For the small-to-medium GNRs group where experimental data is available (section 6.3), the illuminating laser's wavenumber is chosen to match common experimental wavelengths of $\lambda_L \in \{532\text{nm}, 785\text{nm}\}$ as well as the commonly reported limit case of $\lambda_L \rightarrow 0\text{nm}$ which is independent of the specific experimental choice of excitation radiation source.

For the verification group (section 6.2.1) as well as the group of medium-to-large AGNRs (section 6.4), the latter's focus being on identifying intergroup fingerprint differences, only the limit case of $\lambda_L \rightarrow 0\text{nm}$ is reported for comparison.

The full set of calculated intensities and cross-sections is available in appendix C.

6.2 | Verification Group with Reference Data

6.2.1 | Ethane

The total Raman intensity is shown in figure 6.1, and the total Raman cross-section is shown in figure 6.2.

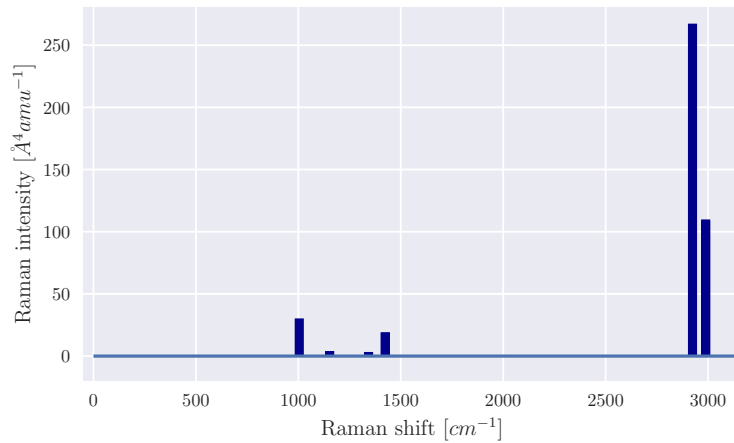


Figure 6.1: Computed Ethane total Raman intensity.

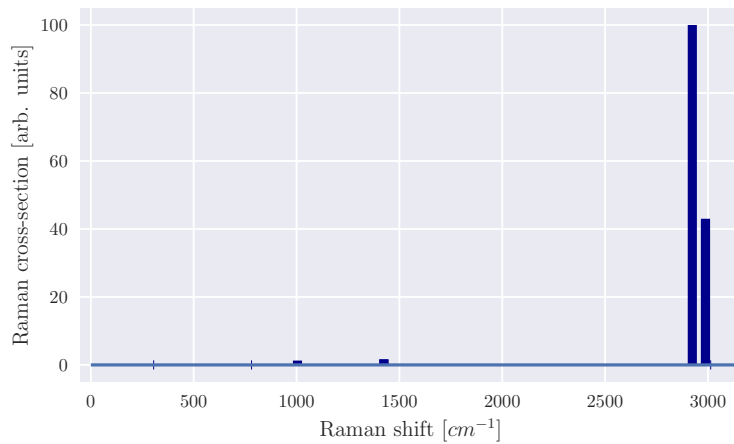


Figure 6.2: Computed Ethane ($\lambda_L = 0\text{nm}$) total Raman cross-section.

6.3 | Small-to-medium GNRs Group with Experimental Data

6.3.1 | 7-AGNR (3 Units)

The total Raman intensity is shown in figure 6.3, and the total Raman cross-sections are shown in figures 6.4, 6.5, and 6.6.

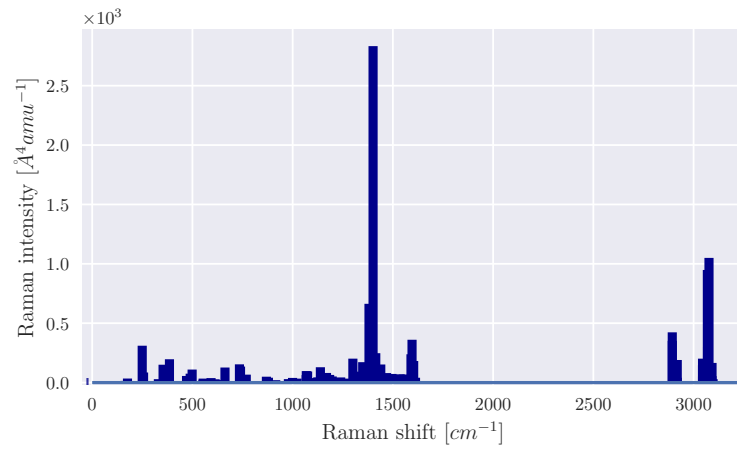


Figure 6.3: Computed 7-AGNR (3 units) total Raman intensity.

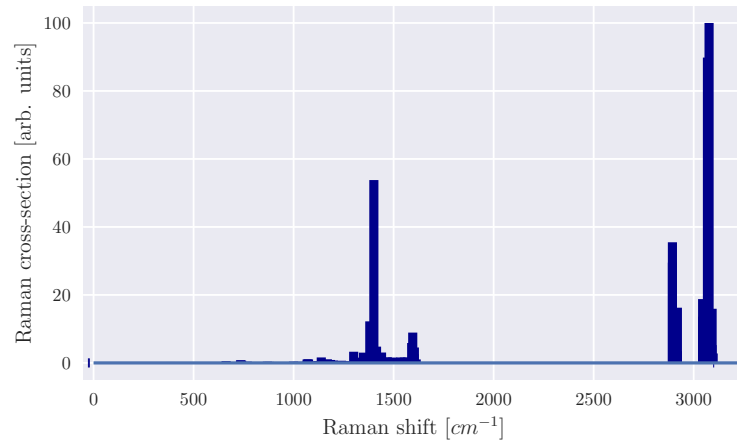


Figure 6.4: Computed 7-AGNR (3 units) ($\lambda_L = 0\text{nm}$) total Raman cross-section.

6.3.2 | 7-AGNR (6 Units)

The total Raman intensity is shown in figure 6.7, and the total Raman cross-sections are shown in figures 6.8, 6.9, and 6.10.

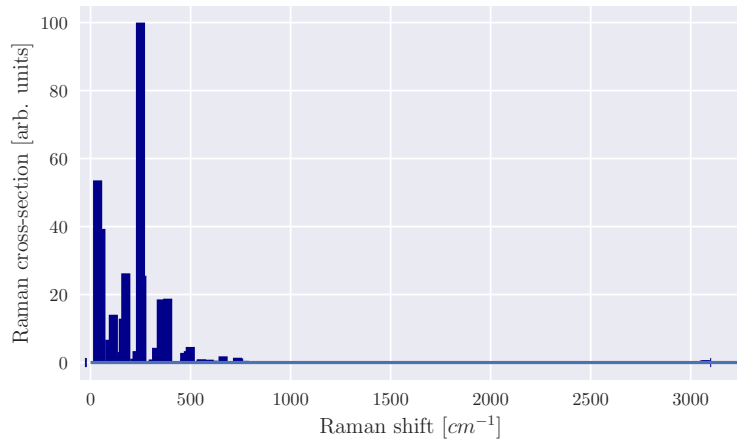


Figure 6.5: Computed 7-AGNR (3 units) ($\lambda_L = 532\text{nm}$) total Raman cross-section.

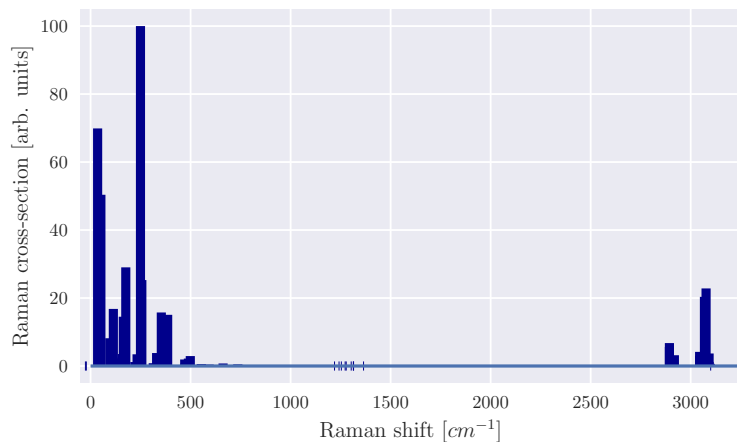


Figure 6.6: Computed 7-AGNR (3 units) ($\lambda_L = 785\text{nm}$) total Raman cross-section.

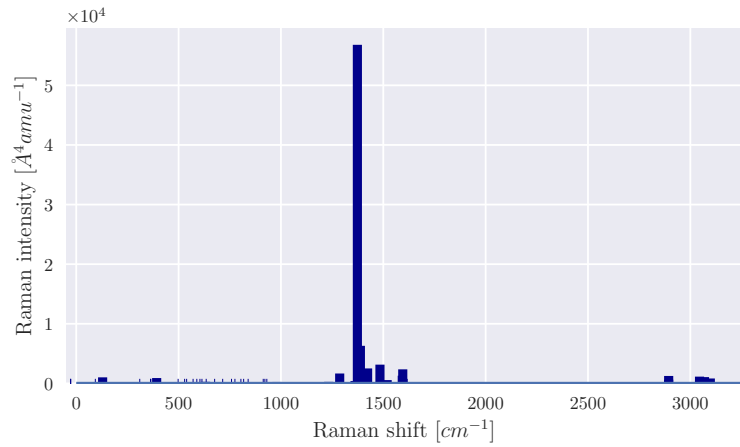


Figure 6.7: Computed 7-AGNR (6 units) total Raman intensity.

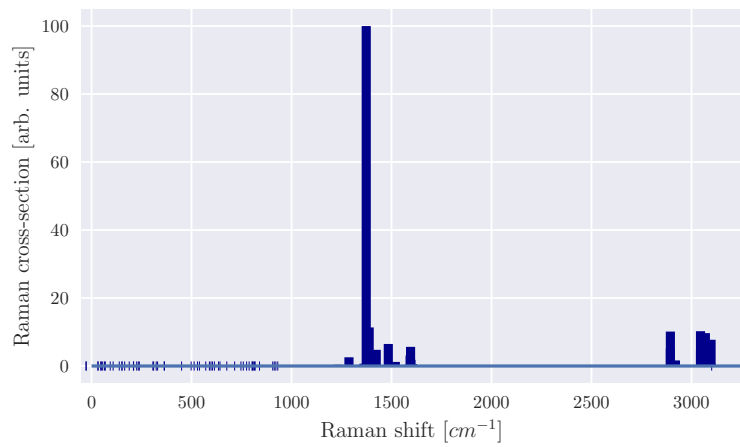


Figure 6.8: Computed 7-AGNR (6 units) ($\lambda_L = 0\text{nm}$) total Raman cross-section.

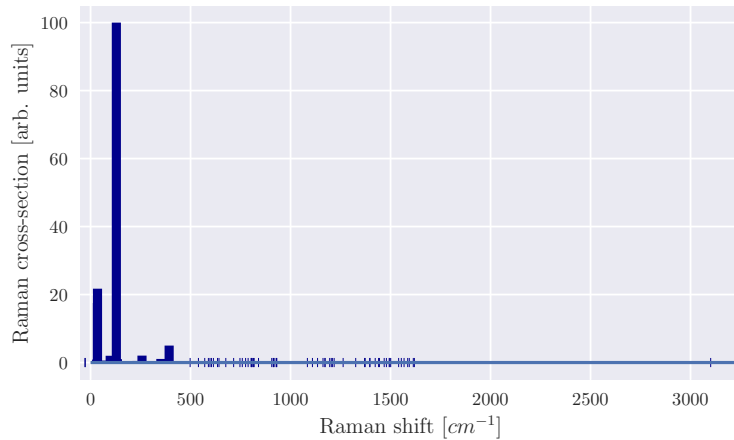


Figure 6.9: Computed 7-AGNR (6 units) ($\lambda_L = 532\text{nm}$) total Raman cross-section.

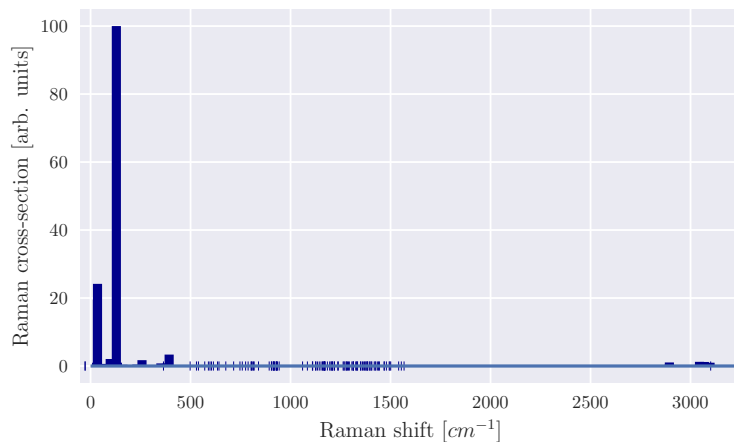


Figure 6.10: Computed 7-AGNR (6 units) ($\lambda_L = 785\text{nm}$) total Raman cross-section.

6.4 | Medium-to-large GNRs Group including Common Defects

6.4.1 | 7-AGNR (12 Units)

The total Raman intensity is shown in figure 6.11, and the total Raman cross-section is shown in figure 6.12.

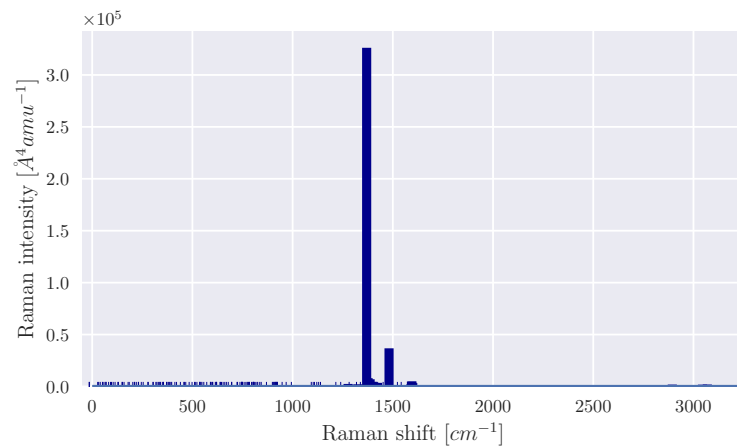


Figure 6.11: Computed 7-AGNR (12 units) total Raman intensity.

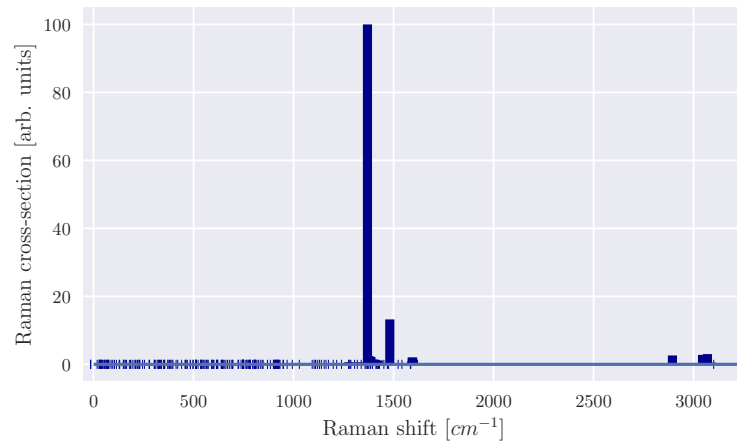


Figure 6.12: Computed 7-AGNR (12 units) ($\lambda_L = 0\text{nm}$) total Raman cross-section.

6.4.2 | 7-AGNR (12 Units): "Bite" Defect

The total Raman intensity is shown in figure 6.13, and the total Raman cross-section is shown in figure 6.14.

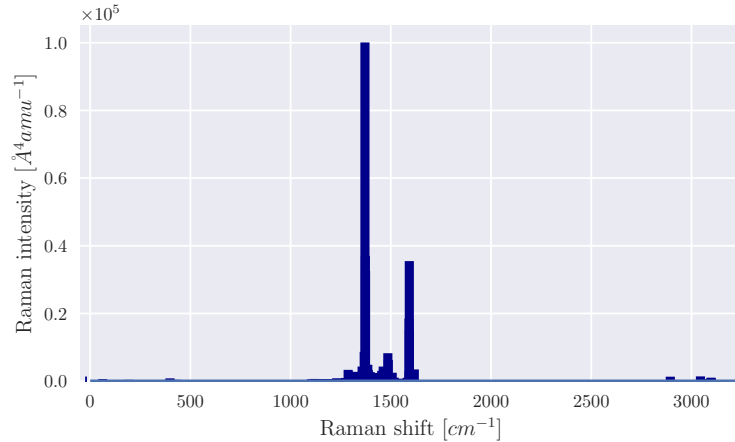


Figure 6.13: Computed 7-AGNR (12 units) "bite" defect total Raman intensity.

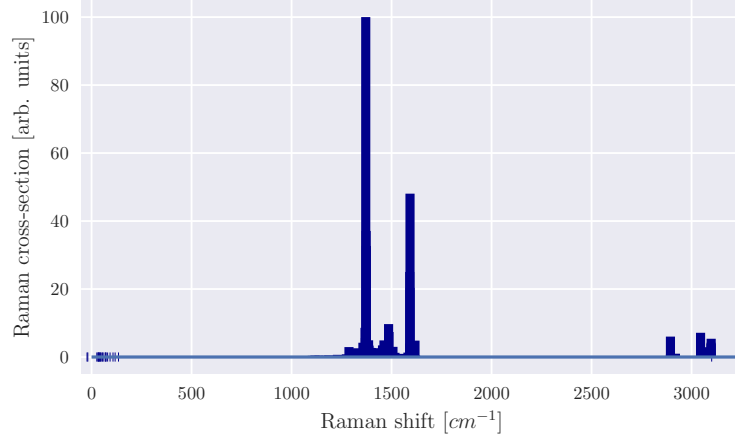


Figure 6.14: Computed 7-AGNR (12 units) "bite" defect ($\lambda_L = 0\text{nm}$) total Raman cross-section.

6.4.3 | 7-AGNR (12 Units): Nitrogen Doping

The total Raman intensity is shown in figure 6.15, and the total Raman cross-section is shown in figure 6.16.

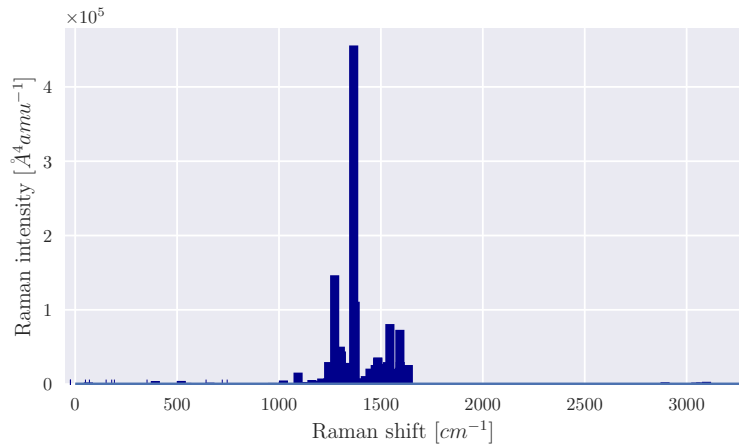


Figure 6.15: Computed 7-AGNR (12 units) nitrogen doping total Raman intensity.

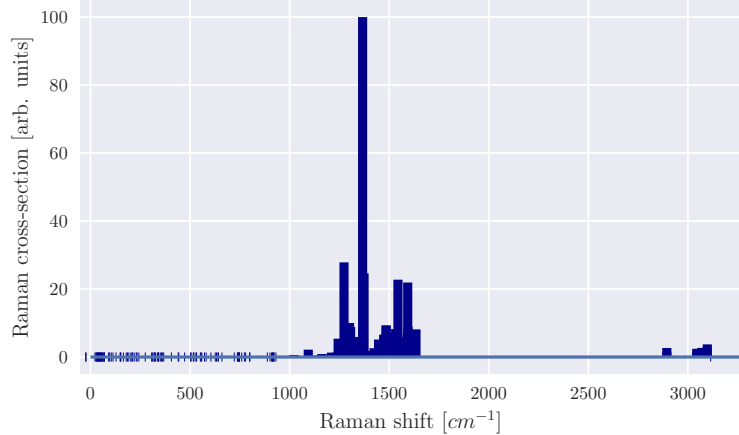


Figure 6.16: Computed 7-AGNR (12 units) nitrogen doping ($\lambda_L = 0 \text{nm}$) total Raman cross-section.

6.4.4 | 7-AGNR (12 Units): Boron and Nitrogen Doping

The total Raman intensity is shown in figure 6.17, and the total Raman cross-section is shown in figure 6.18.

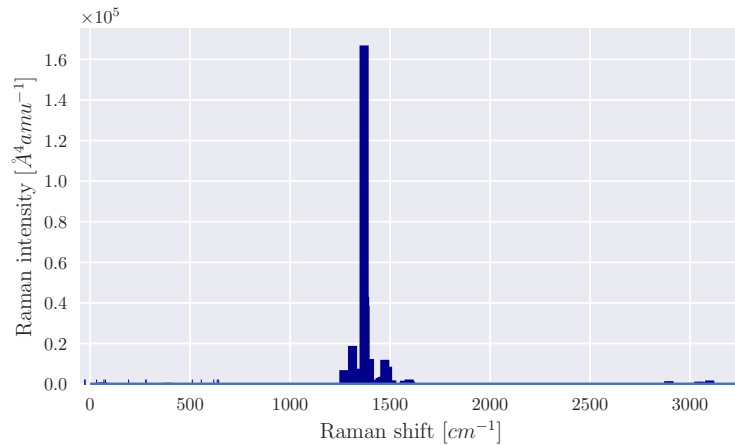


Figure 6.17: Computed 7-AGNR (12 units) nitrogen and boron doping total Raman intensity.

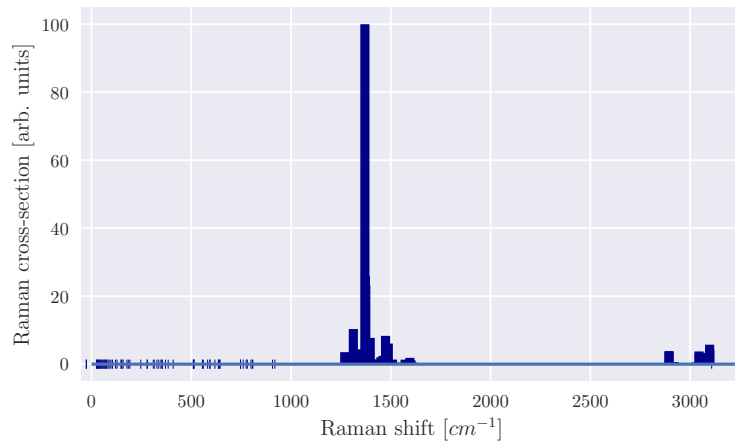


Figure 6.18: Computed 7-AGNR (12 units) nitrogen and boron doping ($\lambda_L = 0\text{nm}$) total Raman cross-section.

Discussion

7.1 | Introduction

This chapter compares the obtained Raman characteristics to the available results from experiments where available and makes an attempt to discuss discrepancies where warranted.

Comparing the Raman spectra of the defective samples with each other, an attempt at identifying fingerprints peculiar to specific defects is made.

Finally, we consider the suitability of the chosen computational workflow in terms of ease of use and performance.

7.2 | Verification Group: Comparison with Reference Data

The molecule Ethane (C_2H_6) was chosen to serve as a verification case for the basic suitability of the chosen computational approach. The published reference data from experiment is given in table 7.1.

Plotting the reference values (table 7.1) with the plotting functionality developed in this study results in figure 7.1a.

Comparing the reference spectrum from figure 7.1a with the computed total Raman intensity as given in figure 7.1b sourced from section 6.2.1 shows a very good match, confirming the viability of the chosen approach.

Mode	ν cm^{-1}			I^{IR} $(\text{D}/\text{\AA})^2 \text{amu}^{-1}$			I^{Raman} $\text{\AA}^4 \text{amu}^{-1}$		
	LDA		GGA	Exp	LDA	GGA	Exp	LDA	GGA
$1A_{1u}$	301	297	303	0.0	0.0	0.0	0.0	0.0	0.0
$1E_u$	780	800	822	0.317	0.200	0.149	0.0	0.0	0.0
$1A_{1g}$	1026	998	1016	0.0	0.0	0.0	9.32	10.7	13.4
$1E_g$	1151	1177	1246	0.0	0.0	0.0	0.347	0.226	0.6
$1A_{2u}$	1323	1354	1438	0.128	0.033	0.059	0.0	0.0	0.0
$2A_{1g}$	1342	1361	1449	0.0	0.0	0.0	0.385	0.121	0.2
$2E_u$	1419	1456	1526	0.656	0.446	0.373	0.0	0.0	0.0
$2E_g$	1420	1457	1552	0.0	0.0	0.0	17.0	16.8	17.8
$2A_{2u}$	2946	2973	3061	1.140	1.395	1.226	0.0	0.0	0.0
$3A_{1g}$	2947	2969	3043	0.0	0.0	0.0	400	368	302
$3E_g$	3011	3022	3175	0.0	0.0	0.0	272	260	290
$3E_u$	3034	3055	3140	1.683	2.694	2.983	0.0	0.0	0.0

Table 7.1: Ethane reference total Raman intensities (Porezag and Pederson, 1996).

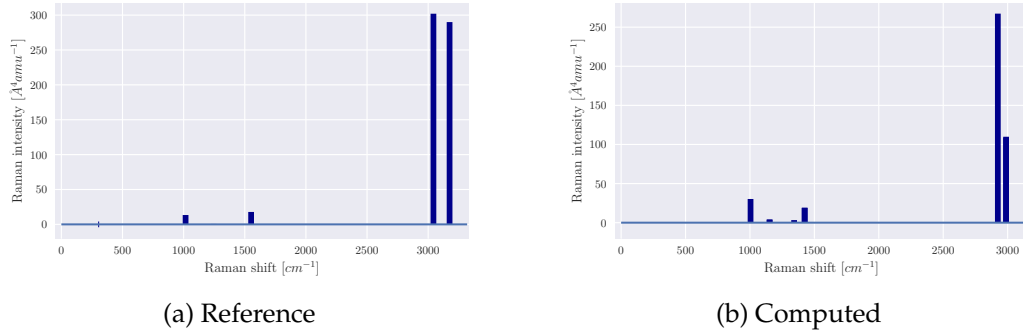


Figure 7.1: Ethane: Comparison of experimental reference (Porezag and Pederson, 1996) and computed total Raman intensity.

7.3 | Small-to-medium GNRs Group: Comparison with Experimental Data

The two sizes (3 units and 6 units) of 7-AGNR were chosen to be representative of simple GNRs typically fabricated by nanotech@surfaces at Empa.

The experimentally obtained total Raman intensity for 7-AGNR (3 units) is shown in figure 7.2a.

While figure 7.2a at first glance shows little resemblance to the 7-AGNR results reported in figure 6.3 in section 6.3 of the preceding chapter, it needs to be noted that the wavenumber cutoff in the experimental data is set at 1800cm^{-1} , while the calculated spectrum contains data up to 3100cm^{-1} . Setting the cutoff for the plot of the computed total Raman intensity to the same 1800cm^{-1} and rescaling the intensity to matching arbitrary units for direct comparison results in figure 7.2b.

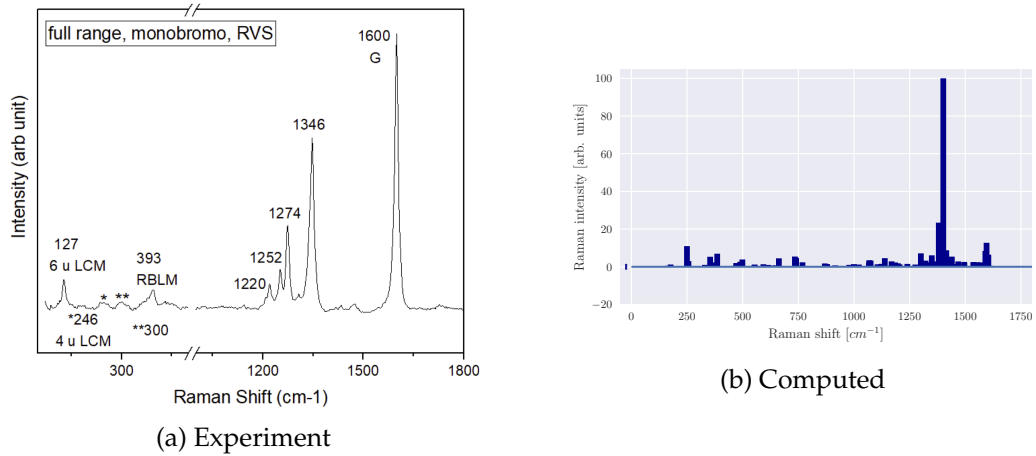


Figure 7.2: 7-AGNR (3 units): Comparison of experimental (Borin Barin, 2020) and computed total Raman intensity.

Comparing computed and experimentally obtained Raman characteristics of 7-AGNR (3 units) reveals some differences: Unlike in the Ethane case considered before in section 7.2, the Raman intensity spectra only match somewhat well: While with 246nm, 393nm, 1346nm, and 1600nm the majority of intensity peaks align reasonably well, especially the intensity of the 1600nm peak is off by a considerable amount.

There are multiple possible reasons for the unsatisfactory match between computed and experimentally obtained Raman intensity spectra, the further investigation of which would go beyond the scope of this report. A shortlist of possible routes of investigation should include the following (Walter and Moseler, 2020): Unlike in the case of organic molecules such as Ethane, the typical excitation wavelengths λ_L fall well within the electronic excitation frequencies of larger molecules such as 7-AGNR, which is completely ignored by the Placzek approximation. Furthermore, no anharmonic effects or mode mixing which both are of second order in the derivative after the vibrational coordinates and are likely to be prevalent in large molecules of the GNR type are considered in the Placzek approximation. Finally, before even considering the shortcomings of the Placzek approximation as such, it could be examined whether stricter convergence criteria in when performing the quantum chemical harmonic approximation for finding the vibrational normal modes improve the precision. Likewise, a higher order finite difference method when calculating the Raman tensor could help to eliminate higher order errors.

7.4 | Medium-to-large GNRs Group: Distinction between Defects

First comparing the obtained Raman characteristics for the larger 12 unit-sized 7-AGNR with the results of the smaller 7-AGNRs studied in the previous group, the obvious consistencies instill confidence in the correctness and reliability of the calculations.

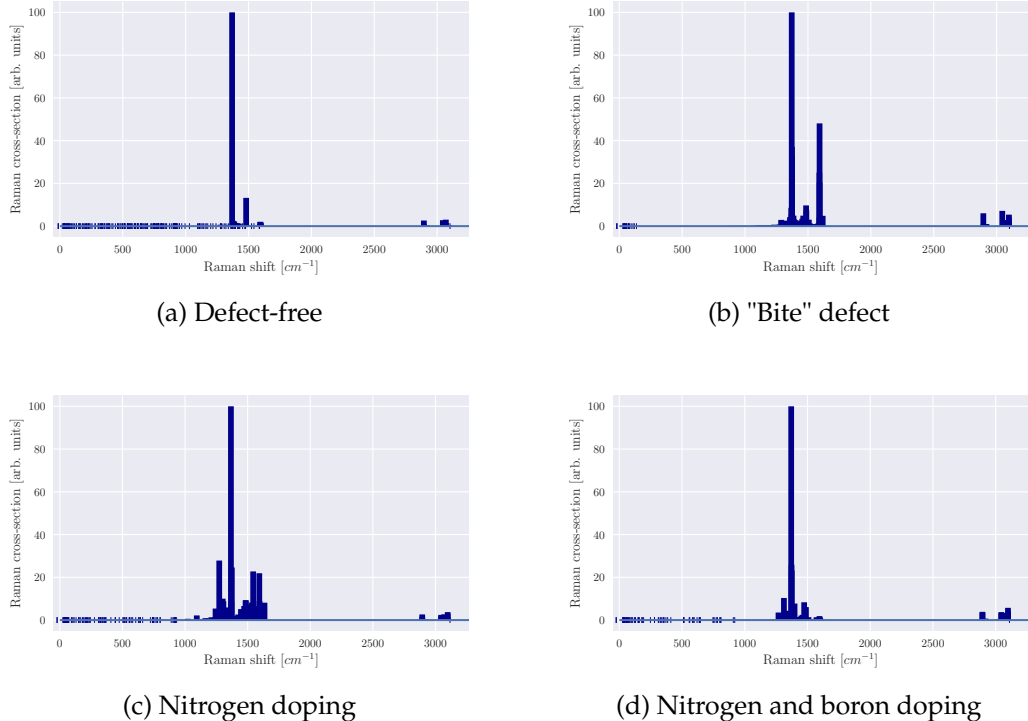


Figure 7.3: 7-ANGR (12 units): Comparison of computed ($\lambda_L = 0\text{nm}$) total Raman cross-section for examined configurations.

Taking a closer look at the similarities and differences between the pristine version of 7-AGNR (12 units) and its three defective siblings allows a favorable assessment of the chosen approach when it comes to identifying fingerprint differences between GNRs with only minor structural differences:

All investigated forms of 7-AGNR (12 units) share a qualitatively similar basic spectrum with two main peak groups, of which the markedly larger first group has a primary peak around 1350cm^{-1} and a secondary peak around 1500cm^{-1} , while the smaller second group has several minor peaks around 3000cm^{-1} .

As figure 7.3 compiled from section 6.4 clearly shows, the four studied forms of 7-AGNR (12 units) can be differentiated by their respective Raman cross-sections:

The "bite" defect form of 7-AGNR (12 units) shows a basic spectrum almost similar to the pristine version's, but with a distinct amplification of the peak around 1600cm^{-1} .

Second under investigation, the nitrogen doping defect form of 7-AGNR (12 units), while being noisier overall, adds a new secondary peak at 1250cm^{-1} while reducing the 1500cm^{-1} peak and having a both somewhat amplified and broadened peak around 1600cm^{-1} .

Finally, the nitrogen plus boron doping defect form of 7-AGNR (12 units), while showing more noise in the two peak groups than the pristine version, has all peaks except the main 1350cm^{-1} peak almost completely suppressed.

In summary, the calculated Raman characteristics allow identifying the examined molecules as members of the 7-AGNR family, while a clear distinction between the pristine form and each of the studied three common defect types is easily possible.

7.5 | Quantum Chemical Calculations with CP2K

The quantum chemical part of the computations performed with CP2K was performed without encountering any stability or performance issues. With a vibrational analysis requiring calculation of the molecular energy for a positive and a negative displacement per atom per dimension, the density functional theory based calculations run in the order of $\mathcal{O}(6n + 1)$ where n is the number of atoms in a molecule. These calculations thus are relatively expensive with growing molecule size and consume considerable compute time: While geometry optimizations run in the order of minutes to hours on 4 nodes of the Swiss National Supercomputing Centre's Piz Daint supercomputer with 12 cores (Intel Xeon E5-2690v3) each, a vibrational analysis for the molecule sizes found in this study runs in the order of several hours on 24-48 nodes of the same supercomputer.

7.6 | Computing Raman Characteristics with Python and NumPy

Implementing the calculation of Raman intensities and cross-sections by way of the Placzek approximation using Python with NumPy poses no stability or performance issues. Running the complete code including the parsing, computation and output plotting reliably takes in the order of seconds on a single core of an Intel Core i9-8950HK (Coffee Lake) laptop system.

Conclusion

The chosen computational approach to compute Raman characteristics using the density functional theory based harmonic approximation for molecule vibrational normal modes and the Placzek approximation to compute the Raman tensor invariants is shown to be viable in principle.

While very close for small molecules, the similarity match between calculated and experimentally measured Raman characteristics is not perfect for larger molecules such as GNRs. Further calculations are required to determine whether higher numerical and quantum chemical precision when determining the molecule vibrational normal modes would increase the overlap of computed Raman characteristics with experimental data or if the Placzek approximation suffers from too many inherent simplifications to make it an ideal choice for larger molecules of the GNR class.

The chosen method however seems very well suited to identifying and clearly distinguishing specific fingerprint patterns of defects commonly occurring in the bottom-up fabrication of GNRs. This is all the more impressive considering the differences between the studied sample molecules are in the low single-digit percentage range in terms of both molecular mass and overall atom count.

References

- XYZ (format) - Open Babel. http://openbabel.org/wiki/XYZ_%28format%29.
- A. M Affoune, B. L. V Prasad, Hirohiko Sato, Toshiaki Enoki, Yutaka Kaburagi, and Yoshihiro Hishiyama. Experimental evidence of a single nano-graphene. *Chemical Physics Letters*, 348(1):17–20, November 2001. ISSN 0009-2614. doi:10.1016/S0009-2614(01)01066-1.
- Verónica Barone, Oded Hod, and Gustavo E. Scuseria. Electronic Structure and Stability of Semiconducting Graphene Nanoribbons. *Nano Letters*, 6(12):2748–2754, December 2006. ISSN 1530-6984. doi:10.1021/nl0617033.
- Stefano Baroni, Stefano de Gironcoli, Andrea Dal Corso, and Paolo Giannozzi. Phonons and related crystal properties from density-functional perturbation theory. *Reviews of Modern Physics*, 73(2):515–562, July 2001. doi:10.1103/RevModPhys.73.515.
- Claire Berger, Zhimin Song, Xuebin Li, Xiaosong Wu, Nate Brown, Cécile Naud, Didier Mayou, Tianbo Li, Joanna Hass, Alexei N. Marchenkov, Edward H. Conrad, Phillip N. First, and Walt A. de Heer. Electronic Confinement and Coherence in Patterned Epitaxial Graphene. *Science*, 312(5777):1191–1196, May 2006. ISSN 0036-8075, 1095-9203. doi:10.1126/science.1125925.
- Gabriela Borin Barin. Experimentally measured Raman spectrum of finite 7-AGNR, April 2020.
- Hao Bu, Yunfei Chen, Min Zou, Hong Yi, Kedong Bi, and Zhonghua Ni. Atomistic simulations of mechanical properties of graphene nanoribbons. *Physics Letters A*, 373(37):3359–3362, September 2009. ISSN 0375-9601. doi:10.1016/j.physleta.2009.07.048.
- Jinming Cai, Pascal Ruffieux, Rached Jaafar, Marco Bieri, Thomas Braun, Stephan Blankenburg, Matthias Muoth, Ari P. Seitsonen, Moussa Saleh, Xinliang Feng, Klaus Müllen, and Roman Fasel. Atomically precise bottom-up fabrication of graphene nanoribbons. *Nature*, 466(7305):470–473, July 2010. ISSN 1476-4687. doi:10.1038/nature09211.
- Abraham G. Cano-Márquez, Fernando J. Rodríguez-Macías, Jessica Campos-Delgado, Claudia G. Espinosa-González, Ferdinando Tristán-López, Daniel Ramírez-González, David A. Cullen, David J.

- Smith, Mauricio Terrones, and Yadira I. Vega-Cantú. Ex-MWNTs: Graphene Sheets and Ribbons Produced by Lithium Intercalation and Exfoliation of Carbon Nanotubes. *Nano Letters*, 9(4):1527–1533, April 2009. ISSN 1530-6984, 1530-6992. doi:10.1021/nl803585s.
- Michele Ceriotti, Fabio Pietrucci, and Marco Bernasconi. Ab initio study of the vibrational properties of crystalline TeO₂: The α , β , and γ phases. *Physical Review B*, 73:104304, March 2006. doi:10.1103/PhysRevB.73.104304.
- Zhihong Chen, Yu-Ming Lin, Michael J. Rooks, and Phaedon Avouris. Graphene nano-ribbon electronics. *Physica E: Low-dimensional Systems and Nanostructures*, 40(2):228–232, December 2007. ISSN 1386-9477. doi:10.1016/j.physe.2007.06.020.
- Rui Cheng, Jingwei Bai, Lei Liao, Hailong Zhou, Yu Chen, Lixin Liu, Yung-Chen Lin, Shan Jiang, Yu Huang, and Xiangfeng Duan. High-frequency self-aligned graphene transistors with transferred gate stacks. *Proceedings of the National Academy of Sciences*, 109(29):11588–11592, July 2012. ISSN 0027-8424, 1091-6490. doi:10.1073/pnas.1205696109.
- Shibin Deng, Weigao Xu, Jinying Wang, Xi Ling, Juanxia Wu, Liming Xie, Jing Kong, Mildred S. Dresselhaus, and Jin Zhang. Direct measurement of the Raman enhancement factor of rhodamine 6G on graphene under resonant excitation. *Nano Research*, 7(9):1271–1279, September 2014. ISSN 1998-0124, 1998-0000. doi:10.1007/s12274-014-0490-3.
- Mitsutaka Fujita, Katsunori Wakabayashi, Kyoko Nakada, and Koichi Kusakabe. Peculiar Localized State at Zigzag Graphite Edge. *Journal of the Physical Society of Japan*, 65(7):1920–1923, July 1996. ISSN 0031-9015. doi:10.1143/JPSJ.65.1920.
- A. K. Geim and K. S. Novoselov. The rise of graphene. *Nature Materials*, 6(3):183–191, March 2007. ISSN 1476-4660. doi:10.1038/nmat1849.
- S. K. Georgantzinos, G. I. Giannopoulos, D. E. Katsareas, P. A. Kakavas, and N. K. Anifantis. Size-dependent non-linear mechanical properties of graphene nanoribbons. *Computational Materials Science*, 50(7):2057–2062, May 2011. ISSN 0927-0256. doi:10.1016/j.commatsci.2011.02.008.
- Marcus D. Hanwell, Donald E. Curtis, David C. Lonie, Tim Vandermeersch, Eva Zurek, and Geoffrey R. Hutchison. Avogadro: An advanced semantic chemical editor, visualization, and analysis platform. *Journal of Cheminformatics*, 4(1):17, August 2012. ISSN 1758-2946. doi:10.1186/1758-2946-4-17.
- Ask Hjorth Larsen, Jens Jørgen Mortensen, Jakob Blomqvist, Ivano E Castelli, Rune Christensen, Marcin Dułak, Jesper Friis, Michael N Groves, Bjørk Hammer, Cory Hargus, Eric D Hermes, Paul C Jennings, Peter Bjerre Jensen, James Kermode, John R Kitchin, Esben Leonhard Kolsbjerg, Joseph Kubal, Kristen Kaasbjerg, Steen Lysgaard, Jón Bergmann Maronsson, Tristan Maxson, Thomas Olsen, Lars Pastewka, Andrew Peterson, Carsten Rostgaard, Jakob Schiøtz, Ole Schütt, Mikkel Strange, Kristian S Thygesen, Tejs Vegge, Lasse Vilhelmsen, Michael Walter, Zhenhua Zeng, and Karsten W Jacobsen. The atomic simulation environment—a Python library for working with atoms. *Journal of Physics: Condensed Matter*, 29(27):273002, July 2017. ISSN 0953-8984, 1361-648X. doi:10.1088/1361-648X/aa680e.
- Beat Hubmann. Simulating Raman spectra: A CP2K-based implementation and its application to defective graphene nanoribbons. August 2020. doi:10.5281/zenodo.4016745.

- Jürg Hutter, Marcella Iannuzzi, Florian Schiffmann, and Joost VandeVondele. Cp2k: Atomistic simulations of condensed matter systems. *WIREs Computational Molecular Science*, 4(1):15–25, 2014. ISSN 1759-0884. doi:10.1002/wcms.1159.
- Kinam Kim, Jae-Young Choi, Taek Kim, Seong-Ho Cho, and Hyun-Jong Chung. A role for graphene in silicon-based semiconductor devices. *Nature*, 479(7373):338–344, November 2011. ISSN 1476-4687. doi:10.1038/nature10680.
- D. J. Klein. Graphitic polymer strips with edge states. *Chemical Physics Letters*, 217(3):261–265, January 1994. ISSN 0009-2614. doi:10.1016/0009-2614(93)E1378-T.
- H. W. Kroto, J. R. Heath, S. C. O'Brien, R. F. Curl, and R. E. Smalley. C 60 : Buckminsterfullerene. *Nature*, 318(6042):162–163, November 1985. ISSN 1476-4687. doi:10.1038/318162a0.
- Barbara Lafuente, R. T. Downs, H. Yang, and N. Stone. 1. *The Power of Databases: The RRUFF Project*. De Gruyter, November 2015. ISBN 978-3-11-041710-4. doi:10.1515/9783110417104-003.
- Jayeeta Lahiri, You Lin, Pinar Bozkurt, Ivan I. Oleynik, and Matthias Batzill. An extended defect in graphene as a metallic wire. *Nature Nanotechnology*, 5(5):326–329, May 2010. ISSN 1748-3395. doi:10.1038/nnano.2010.53.
- Qiaohao Liang, Shyam Dwaraknath, and Kristin A. Persson. High-throughput computation and evaluation of raman spectra. *Scientific Data*, 6(1):135, July 2019. ISSN 2052-4463. doi:10.1038/s41597-019-0138-y.
- Ming-Fa Lin and Feng-Lin Shyu. Optical Properties of Nanographite Ribbons. *Journal of the Physical Society of Japan*, 69(11):3529–3532, November 2000. ISSN 0031-9015. doi:10.1143/JPSJ.69.3529.
- Derek A. Long. *The Raman Effect*. John Wiley & Sons, Ltd, Chichester, UK, April 2002. ISBN 978-0-471-49028-9 978-0-470-84576-9. doi:10.1002/0470845767.
- Sandra Luber, Marcella Iannuzzi, and Jürg Hutter. Raman spectra from ab initio molecular dynamics and its application to liquid S-methyloxirane. *The Journal of Chemical Physics*, 141(9):094503, September 2014. ISSN 0021-9606. doi:10.1063/1.4894425.
- L. M. Malard, M. A. Pimenta, G. Dresselhaus, and M. S. Dresselhaus. Raman spectroscopy in graphene. *Physics Reports*, 473(5):51–87, April 2009. ISSN 0370-1573. doi:10.1016/j.physrep.2009.02.003.
- Hery Mitsutake, Ronei Poppi, and Márcia Breitkreitz. Raman Imaging Spectroscopy: History, Fundamentals and Current Scenario of the Technique. *Journal of the Brazilian Chemical Society*, 2019. ISSN 01035053. doi:10.21577/0103-5053.20190116.
- H. Murayama and T. Maeda. A novel form of filamentous graphite. *Nature*, 345(6278):791–793, June 1990. ISSN 1476-4687. doi:10.1038/345791a0.
- Kyoko Nakada, Mitsutaka Fujita, Gene Dresselhaus, and Mildred S. Dresselhaus. Edge state in graphene ribbons: Nanometer size effect and edge shape dependence. *Physical Review B*, 54(24):17954–17961, December 1996. doi:10.1103/PhysRevB.54.17954.
- M. Neek-Amal and F. M. Peeters. Graphene nanoribbons subjected to axial stress. *Physical Review B*, 82(8):085432, August 2010. doi:10.1103/PhysRevB.82.085432.

- Johannes Neugebauer, Markus Reiher, Carsten Kind, and Bernd A. Hess. Quantum chemical calculation of vibrational spectra of large molecules - Raman and IR spectra for Buckminsterfullerene. *Journal of Computational Chemistry*, 23(9):895–910, July 2002. ISSN 0192-8651, 1096-987X. doi:10.1002/jcc.10089.
- K. S. Novoselov, A. K. Geim, S. V. Morozov, S. V. Dubonos, Y. Zhang, and D. Jiang. Room-temperature electric field effect and carrier-type inversion in graphene films. *arXiv:cond-mat/0410631*, October 2004.
- Jan Overbeck, Gabriela Borin Barin, Colin Daniels, Mickael L. Perrin, Oliver Braun, Qiang Sun, Rimah Darawish, Marta De Luca, Xiao-Ye Wang, Tim Dumslaff, Akimitsu Narita, Klaus Müllen, Pascal Ruffieux, Vincent Meunier, Roman Fasel, and Michel Calame. A Universal Length-Dependent Vibrational Mode in Graphene Nanoribbons. *ACS Nano*, 13(11):13083–13091, November 2019. ISSN 1936-0851. doi:10.1021/acsnano.9b05817.
- Michele Pizzochero, Kristiāns Černevičs, Gabriela Borin Barin, Shiyong Wang, Pascal Ruffieux, Roman Fasel, and Oleg V. Yazyev. Quantum Electronic Transport Across "Bite" Defects in Graphene Nanoribbons. *arXiv:2006.15075 [cond-mat]*, June 2020.
- G Placzek. *Rayleigh-Streuung und Raman-Effekt*. Akademische Verlagsgesellschaft, Leipzig, 1934.
- Dirk Porezag and Mark R. Pederson. Infrared intensities and Raman-scattering activities within density-functional theory. *Physical Review B*, 54(11):7830–7836, September 1996. ISSN 0163-1829, 1095-3795. doi:10.1103/PhysRevB.54.7830.
- C. V. Raman and K. S. Krishnan. A New Type of Secondary Radiation. *Nature*, 121(3048):501–502, March 1928. ISSN 1476-4687. doi:10.1038/121501c0.
- M. Reiher, J. Neugebauer, and B. A. Hess. Quantum Chemical Calculation of Raman Intensities for Large Molecules: The Photoisomerization of $[\text{Fe}'\text{S}4'(\text{PR}_3)2(\text{N}_2\text{H}_2)]$ ('S '2- = 1,2-bis(2-Mercaptophenylthio)-4 Ethane(2-)). *Zeitschrift für Physikalische Chemie*, 217(2-2003):91–104, February 2003. ISSN 0942-9352. doi:10.1524/zpch.217.2.91.22616.
- Tatsuya Sasaki, Yasuhiro Yamada, and Satoshi Sato. Quantitative Analysis of Zigzag and Armchair Edges on Carbon Materials with and without Pentagons Using Infrared Spectroscopy. *Analytical Chemistry*, 90(18):10724–10731, September 2018. ISSN 0003-2700. doi:10.1021/acs.analchem.8b00949.
- Frank Schwierz. Graphene Transistors: Status, Prospects, and Problems. *Proceedings of the IEEE*, 101(7):1567–1584, July 2013. ISSN 1558-2256. doi:10.1109/JPROC.2013.2257633.
- Leopold Talirz and Carlo A. Pignedoli. Electronic Structure of Atomically Precise Graphene Nanoribbons. In Wanda Andreoni and Sidney Yip, editors, *Handbook of Materials Modeling: Applications: Current and Emerging Materials*, pages 685–719. Springer International Publishing, Cham, 2020. ISBN 978-3-319-44680-6. doi:10.1007/978-3-319-44680-6_41.
- Martin Thomas, Martin Brehm, Reinhold Fligg, Peter Vöhringer, and Barbara Kirchner. Computing vibrational spectra from ab initio molecular dynamics. *Physical Chemistry Chemical Physics*, 15(18):6608, 2013. ISSN 1463-9076, 1463-9084. doi:10.1039/c3cp44302g.
- Stefan van der Walt, S. Chris Colbert, and Gael Varoquaux. The NumPy Array: A Structure for Efficient Numerical Computation. *Computing in Science Engineering*, 13(2):22–30, March 2011. ISSN 1558-366X. doi:10.1109/MCSE.2011.37.

Michael Walter and Michael Moseler. Ab Initio Wavelength-Dependent Raman Spectra: Placzek Approximation and Beyond. *Journal of Chemical Theory and Computation*, 16(1):576–586, January 2020. ISSN 1549-9618. doi:10.1021/acs.jctc.9b00584.

Willes H Weber and R Merlin. *Raman Scattering in Materials Science*. Springer, Berlin; London, 2011. ISBN 978-3-642-08656-4.

Representative CP2K Configuration Files

Geometry Optimization Input File cp2k.inp

```
1 &FORCE_EVAL
2   METHOD Quickstep
3   &DFT
4     BASIS_SET_FILE_NAME ./BR
5     POTENTIAL_FILE_NAME ./GR
6     RESTART_FILE_NAME ./PROJ-RESTART.wfn
7   #   &PRINT
8   #     &MOMENTS
9   #     &END
10  #    &END
11  &QS
12    METHOD GPW
13    EXTRAPOLATION ASPC
14    EXTRAPOLATION_ORDER 3
15    EPS_DEFAULT 1.0E-14
16  #    MAP_CONSISTENT
17  &END QS
18  &MGRID
19    CUTOFF 600
20    NGRIDS 5
21  &END
```

```
22      &SCF
23          MAX_SCF 20
24          SCF_GUESS ATOMIC
25          EPS_SCF 1.0E-9
26      &OT
27          PRECONDITIONER FULL_SINGLE_INVERSE
28          MINIMIZER CG
29      &END
30      &OUTER_SCF
31          MAX_SCF 15
32          EPS_SCF 1.0E-9
33      &END
34      &PRINT
35          &RESTART
36              &EACH
37                  QS_SCF 0
38                  GEO_OPT 1
39              &END
40          ADD_LAST NUMERIC
41          FILENAME RESTART
42      &END
43          &RESTART_HISTORY OFF
44      &END
45      &END
46  &END SCF
47  &XC
48      &XC_FUNCTIONAL PADE
49  &END XC_FUNCTIONAL
50  &END XC
51  &END DFT
52  &SUBSYS
53  &CELL
54      ABC 10 10 10
55  &END
56  &TOPOLOGY
57      COORD_FILE_NAME ./c2h6.xyz
```

```
58      COORDINATE xyz
59      &END
60      &KIND C
61          BASIS_SET TZV2P-MOLOPT-GTH
62          POTENTIAL GTH-PBE-q4
63      &END KIND
64      &KIND H
65          BASIS_SET TZV2P-MOLOPT-GTH
66          POTENTIAL GTH-PBE-q1
67      &END KIND
68      &END SUBSYS
69  &END FORCE_EVAL
70  &GLOBAL
71      PRINT_LEVEL LOW
72      PROJECT PROJ
73 #  RUN_TYPE NORMAL_MODES
74      RUN_TYPE GEO_OPT
75      WALLTIME 86000
76      EXTENDED_FFT_LENGTHS
77  &END GLOBAL
78
79  &MOTION
80      &GEO_OPT
81          MAX_FORCE 0.00005 # 0.0001 a.u. = 0.005 ev/ang
82          MAX_ITER 1600
83          OPTIMIZER BFGS
84      &BFGS
85          TRUST_RADIUS [bohr] 0.1
86      &END
87  &END
88  &END
89
90 #&VIBRATIONAL_ANALYSIS
91 #  NPROC REP 3
92 #  DX 0.005
93 #  INTENSITIES
```

```
94 #      &PRINT
95 #      &PROGRAM_RUN_INFO ON
96 #      &END
97 #      &END
98 #&END
99
100 #&EXT_RESTART
101 # RESTART_FILE_NAME ./PROJ-1.restart
102 #&END
```

Vibrational Analysis Input File cp2k.inp

```
1 &FORCE_EVAL
2   METHOD Quickstep
3   &DFT
4     BASIS_SET_FILE_NAME ./BR
5     POTENTIAL_FILE_NAME ./GR
6     RESTART_FILE_NAME ./PROJ-RESTART.wfn
7     &PRINT
8       &MOMENTS
9     &END
10    &END
11    &QS
12      METHOD GPW
13      EXTRAPOLATION ASPC
14      EXTRAPOLATION_ORDER 3
15      EPS_DEFAULT 1.0E-14
16 #      MAP_CONSISTENT
17    &END QS
18    &MGRID
19      CUTOFF 600
20      NGRIDS 5
21    &END
22    &SCF
23      MAX_SCF 20
```

```
24      SCF_GUESS RESTART
25      EPS_SCF 1.0E-9
26      &OT
27          PRECONDITIONER FULL_SINGLE_INVERSE
28          MINIMIZER CG
29      &END
30      &OUTER_SCF
31          MAX_SCF 15
32          EPS_SCF 1.0E-9
33      &END
34      &PRINT
35          &RESTART
36              &EACH
37                  QS_SCF 0
38                  GEO_OPT 1
39              &END
40          ADD_LAST NUMERIC
41          FILENAME RESTART
42      &END
43      &RESTART_HISTORY OFF
44      &END
45      &END
46  &END SCF
47  &XC
48      &XC_FUNCTIONAL PADE
49  &END XC_FUNCTIONAL
50  &END XC
51  &END DFT
52  &PROPERTIES
53      &LINRES
54          MAX_ITER 2000
55          PRECONDITIONER FULL_ALL
56          EPS 1E-6
57          &POLAR
58          DO_RAMAN T
59      &END
```

```
60      &END
61      &END
62      &SUBSYS
63          &CELL
64              ABC 10 10 10
65          &END
66          &TOPOLOGY
67              COORD_FILE_NAME ./c2h6-opt.xyz
68              COORDINATE xyz
69          &END
70          &KIND C
71              BASIS_SET TZV2P-MOLOPT-GTH
72              POTENTIAL GTH-PBE-q4
73          &END KIND
74          &KIND H
75              BASIS_SET TZV2P-MOLOPT-GTH
76              POTENTIAL GTH-PBE-q1
77          &END KIND
78      &END SUBSYS
79  &END FORCE_EVAL
80  &GLOBAL
81      PRINT_LEVEL LOW
82      PROJECT PROJ
83      RUN_TYPE NORMAL_MODES
84 #  RUN_TYPE GEO_OPT
85      WALLTIME 86000
86      EXTENDED_FFT_LENGTHS
87  &END GLOBAL
88
89  &VIBRATIONAL_ANALYSIS
90      NPROC REP 3
91      DX 0.001
92      INTENSITIES
93      &PRINT
94          &PROGRAM_RUN_INFO ON
95      &END
```

```
96      &END
97  &END
98
99 #&EXT_RESTART
100 # RESTART_FILE_NAME ./PROJ-1.restart
101 #&END
```

Python Source Code Key Excerpts

Computing the Raman Tensor from the Polarizability Tensor

```
1  # FDM 3-point first derivative of polarizability tensors:
2
3  # dx in cp2k is in Bohr, polarizability tensors are in Angstrom^3:
4  bohr2ang = 0.5291772109
5  factor = 1 / (2 * dx * bohr2ang)
6
7  # polarizability tensor derivatives w.r.t. cartesian coordinates
8  # in Angstrom^2:
9  polariz_dxxy = factor * (polarizabilities[:, :, 0, :, :] -
10    polarizabilities[:, :, 1, :, :])
11
12  # Calculating Raman tensor from polarizability tensor derivatives,
13  # normal mode displacements, atomic masses
14
15  polariz_dq = np.einsum('ad...,akd,a->k...', polariz_dxxy,
16    normal_displacements, atom_mass_inv_sqrt)
```

Computing the Placzek Invariants

```

1  # Placzek tensor invariants
2
3  # mean polarizability squared:
4  a_sq = np.square(np.trace(polariz_dq, 0, 2) / 3).reshape((-1,1))
5
6  # anisotropy:
7  gamma_sq = np.zeros((num_normal_modes,1))
8
9  # asymmetric anisotropy:
10 delta_sq = np.zeros_like(gamma_sq)
11
12 for k in range(num_normal_modes):
13     gamma_sq[k] = 0.5 * (np.square(polariz_dq[k][0][0] -
14                             polariz_dq[k][1][1]) -
15                             +np.square(polariz_dq[k][1][1] -
16                             polariz_dq[k][2][2]) +
17                             np.square(polariz_dq[k][2][2] -
18                             polariz_dq[k][0][0])) \
19                             +3 * (np.square(polariz_dq[k][0][1]) +
20                             np.square(polariz_dq[k][1][2]) +
21                             np.square(polariz_dq[k][2][0]))
22     delta_sq[k] = 0.75 * (np.square(polariz_dq[k][0][1] -
23                             polariz_dq[k][1][0]) +
24                             np.square(polariz_dq[k][0][2] -
25                             polariz_dq[k][2][0]) +
26                             np.square(polariz_dq[k][1][2] -
27                             polariz_dq[k][2][1]))

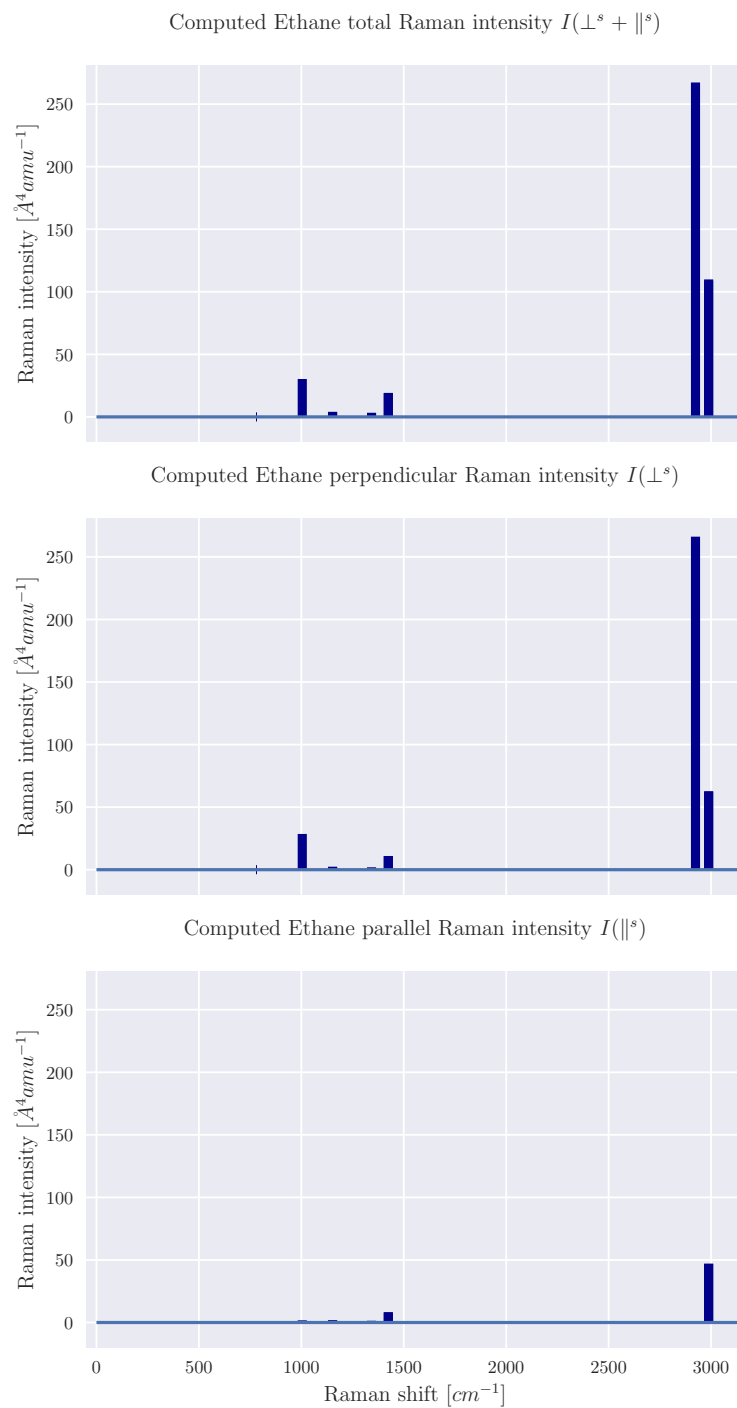
```

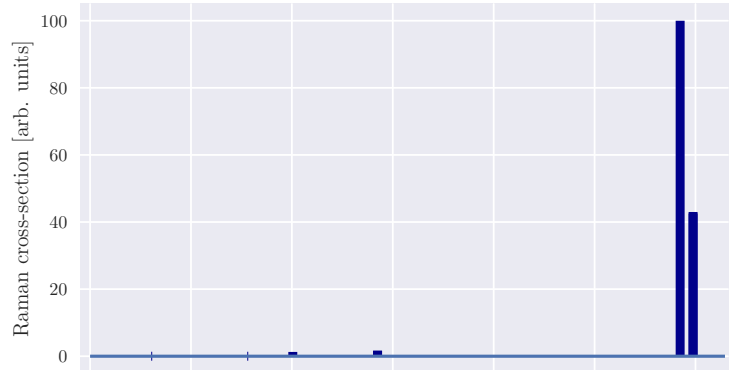
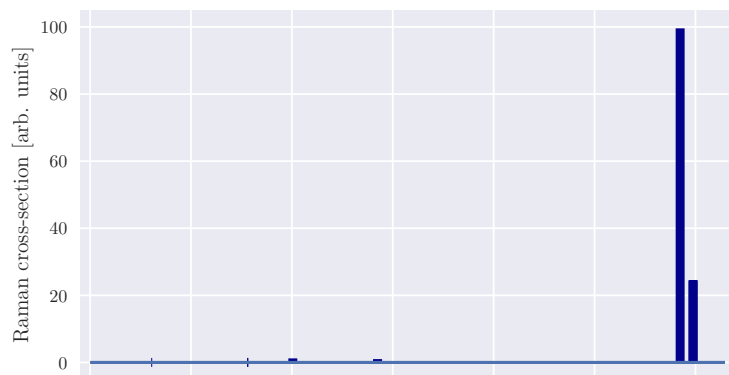
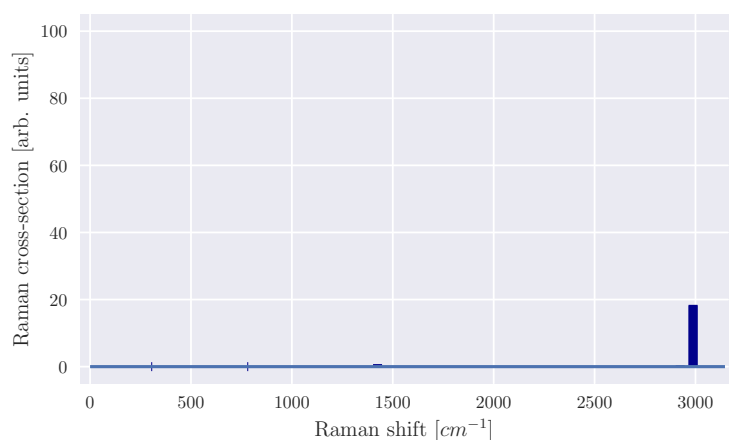
Computing Raman Intensities

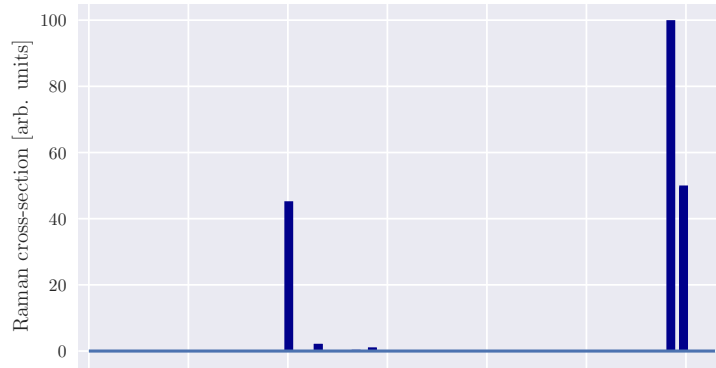
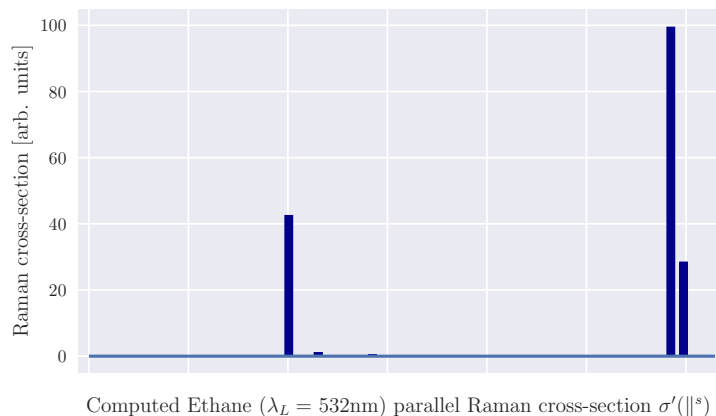
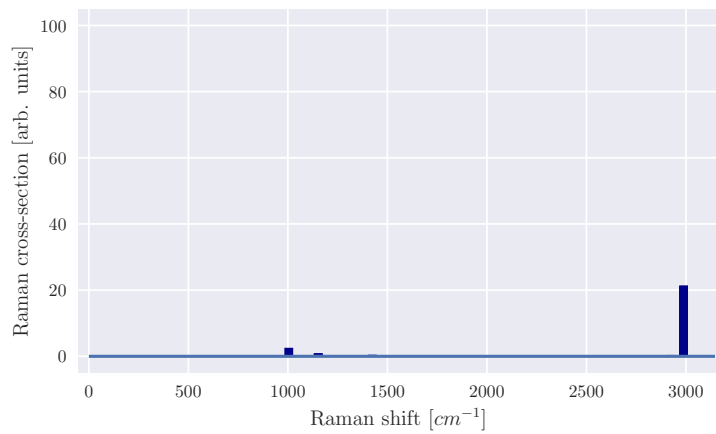
```
1  # calculate absolute Raman intensity: total , perpendicular &
2  # parallel polarized scattering
3
4  I_raman = np.zeros((num_normal_modes,3))
5  for k in range(num_normal_modes):
6      if normal_freqs[k] > 0:  # there are no physical negative
7          normal frequencies
8          I_raman[k] = 45 * a_sq[k] + 7 * gamma_sq[k] + 5 * delta_sq
9              [k], \
10                 45 * a_sq[k] + 4 * gamma_sq[k]
11                 , \
12                 3 * gamma_sq[k] + 5 * delta_sq
13                     [k]
```

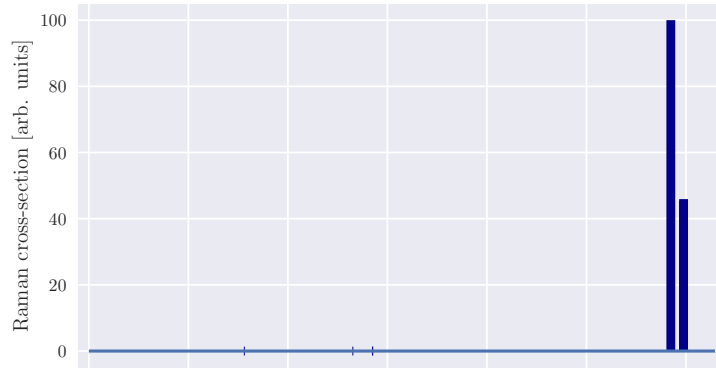
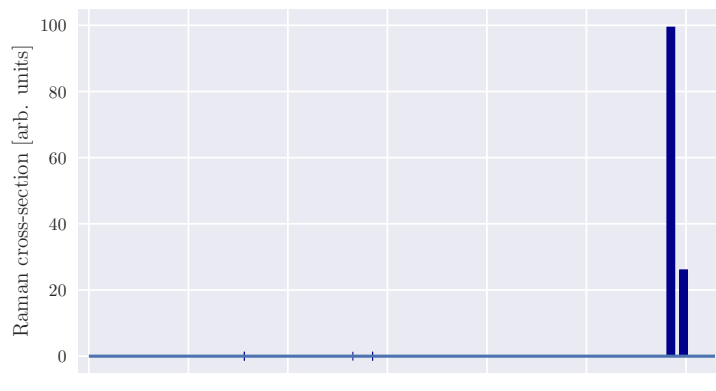
Supplementary Results

Ethane

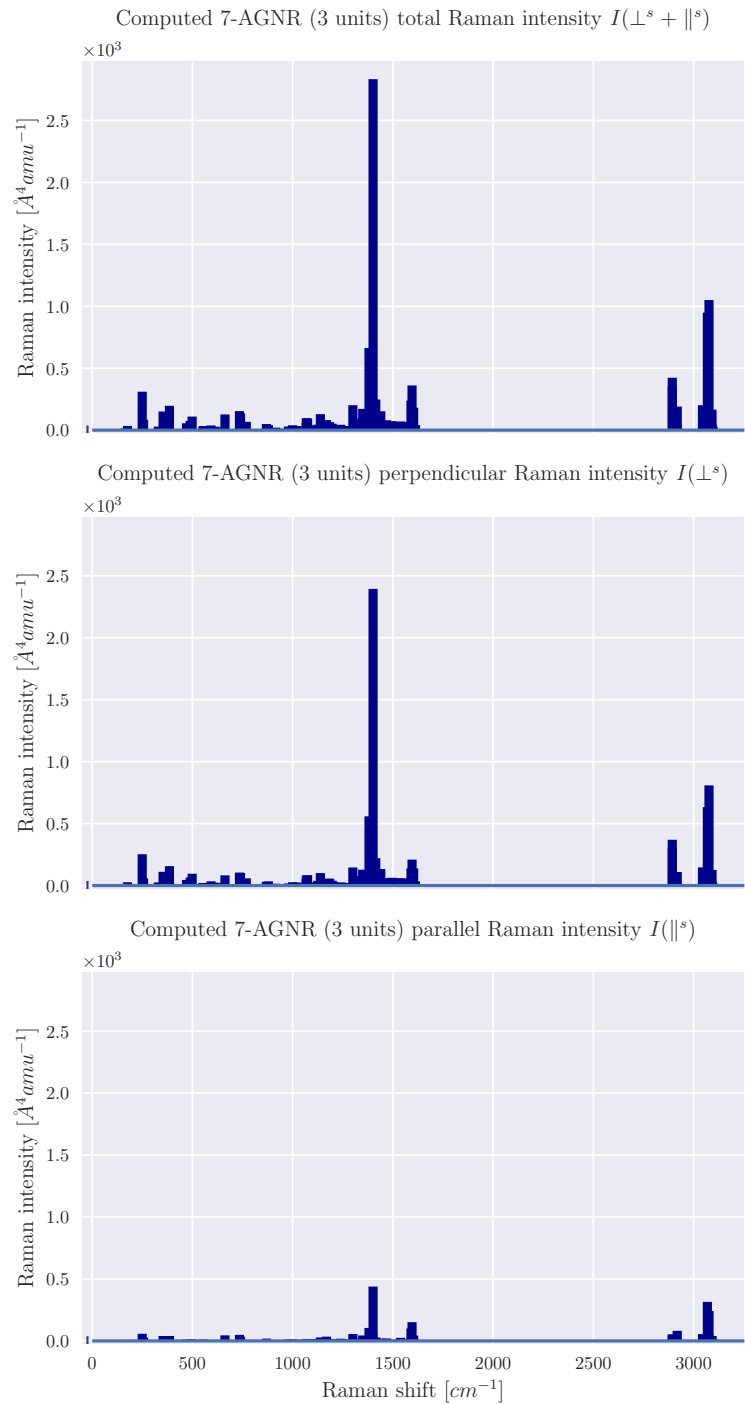


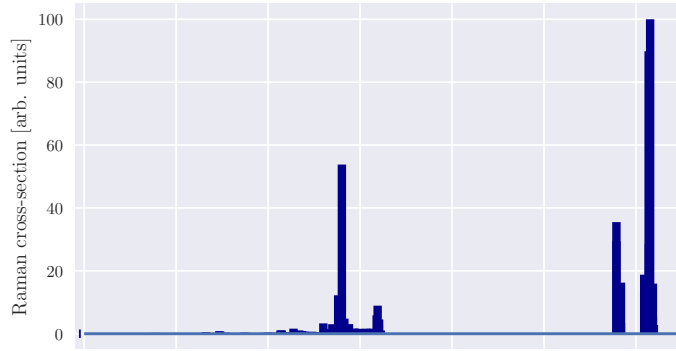
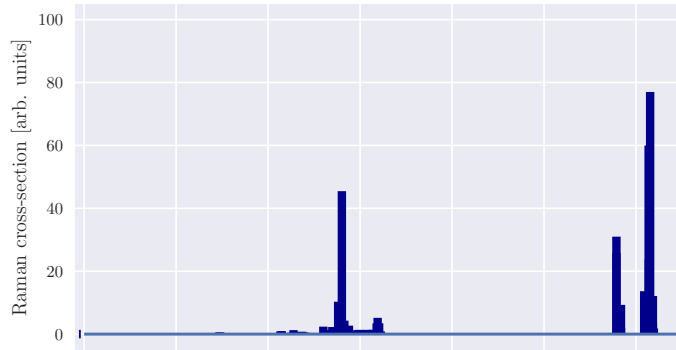
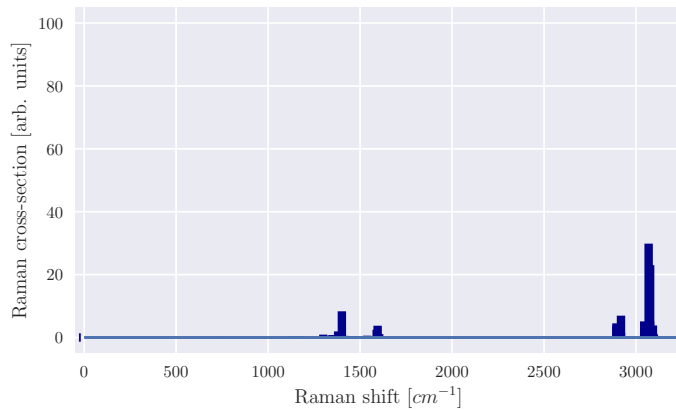
Computed Ethane ($\lambda_L = 0\text{nm}$) total Raman cross-section $\sigma'(\perp^s + \parallel^s)$ Computed Ethane ($\lambda_L = 0\text{nm}$) perpendicular Raman cross-section $\sigma'(\perp^s)$ Computed Ethane ($\lambda_L = 0\text{nm}$) parallel Raman cross-section $\sigma'(\parallel^s)$ 

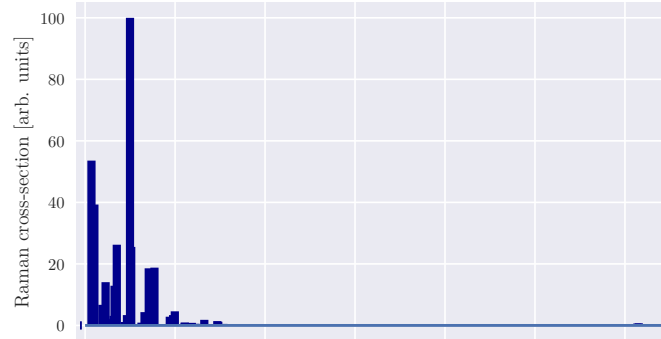
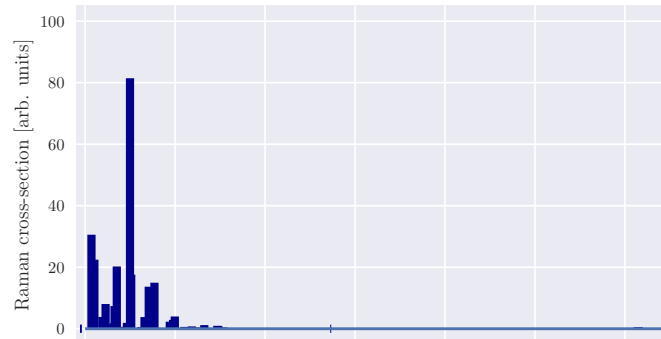
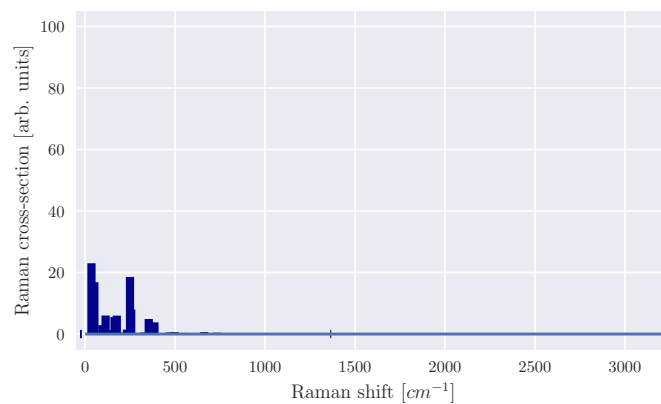
Computed Ethane ($\lambda_L = 532\text{nm}$) total Raman cross-section $\sigma'(\perp^s + \parallel^s)$ Computed Ethane ($\lambda_L = 532\text{nm}$) perpendicular Raman cross-section $\sigma'(\perp^s)$ Computed Ethane ($\lambda_L = 532\text{nm}$) parallel Raman cross-section $\sigma'(\parallel^s)$ 

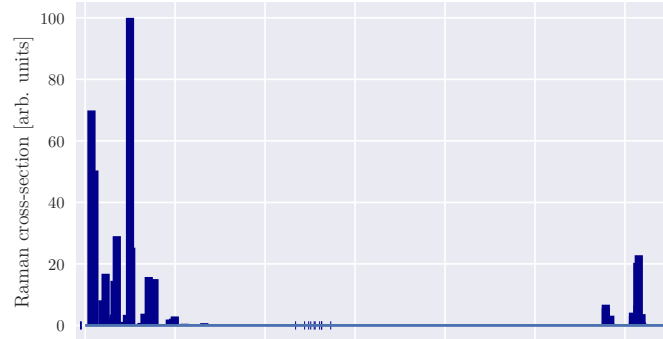
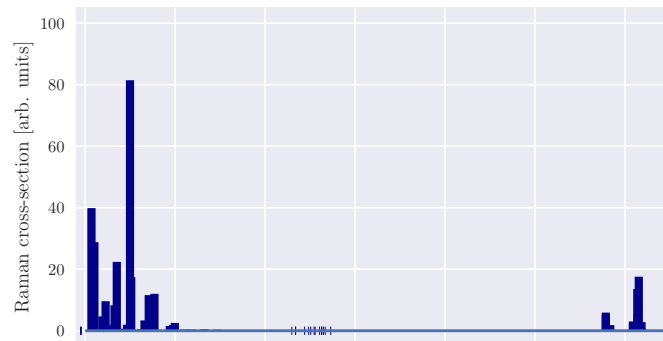
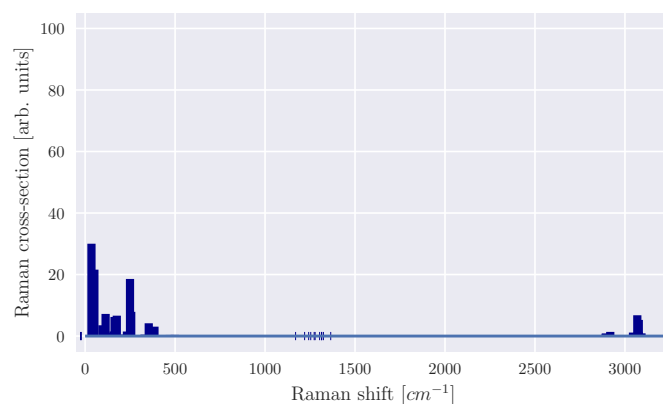
Computed Ethane ($\lambda_L = 785\text{nm}$) total Raman cross-section $\sigma'(\perp^s + \parallel^s)$ Computed Ethane ($\lambda_L = 785\text{nm}$) perpendicular Raman cross-section $\sigma'(\perp^s)$ Computed Ethane ($\lambda_L = 785\text{nm}$) parallel Raman cross-section $\sigma'(\parallel^s)$ 

7-AGNR (3 units)

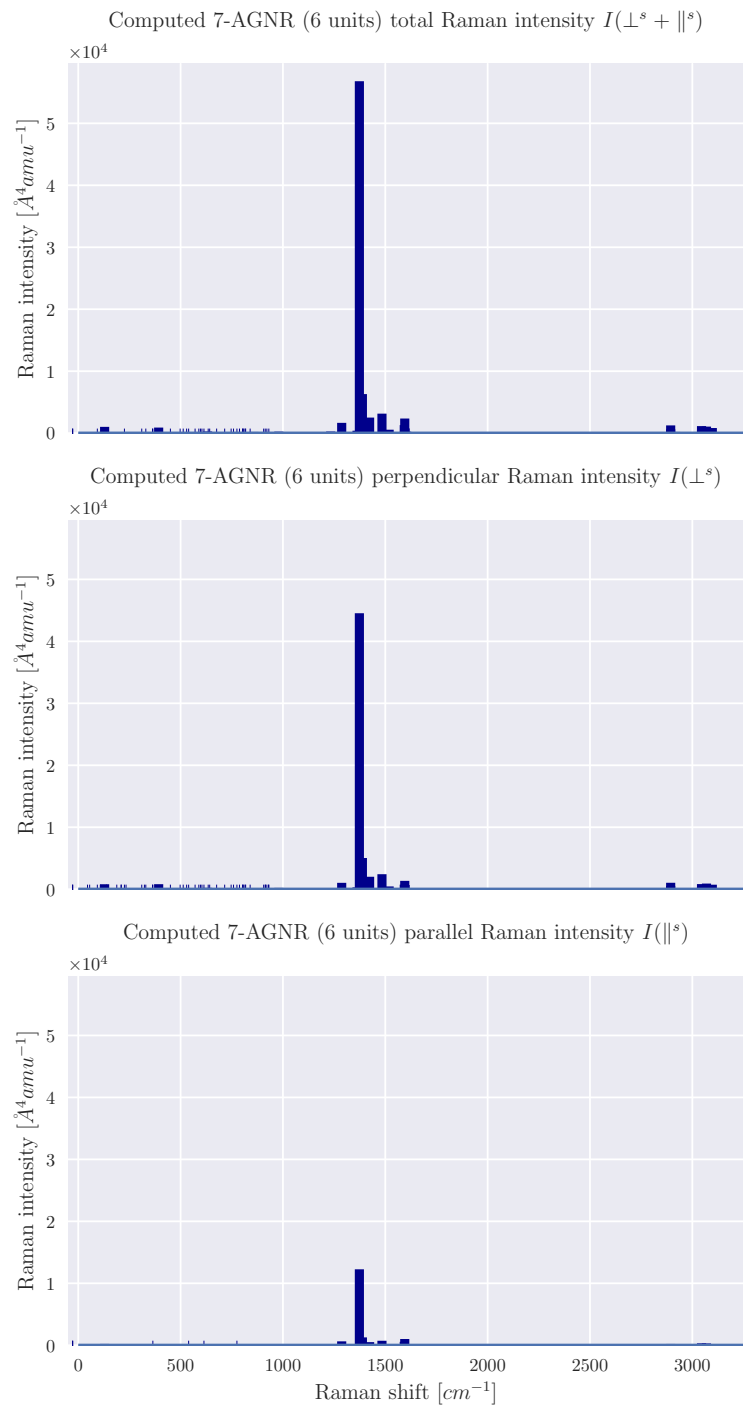


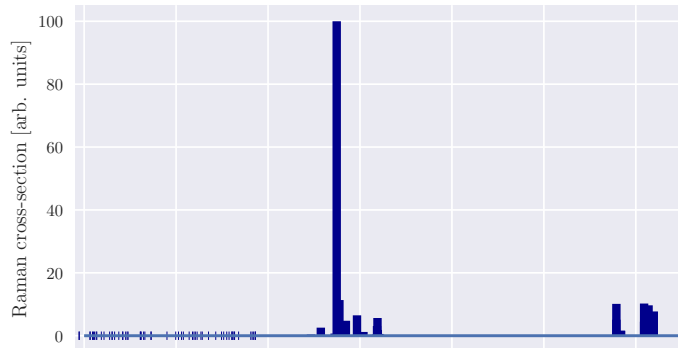
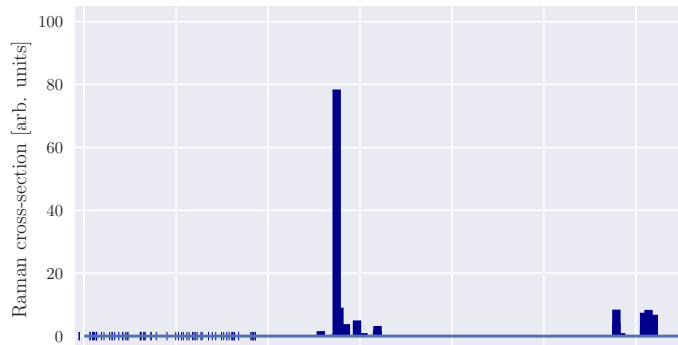
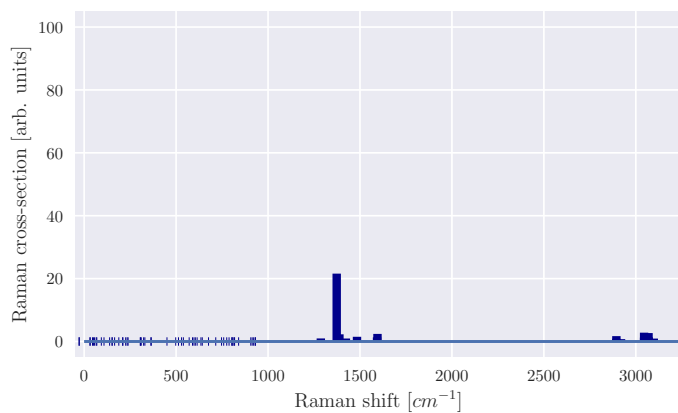
Computed 7-AGNR (3 units) ($\lambda_L = 0\text{nm}$) total Raman cross-section $\sigma'(\perp^s + \parallel^s)$ Computed 7-AGNR (3 units) ($\lambda_L = 0\text{nm}$) perpendicular Raman cross-section $\sigma'(\perp^s)$ Computed 7-AGNR (3 units) ($\lambda_L = 0\text{nm}$) parallel Raman cross-section $\sigma'(\parallel^s)$ 

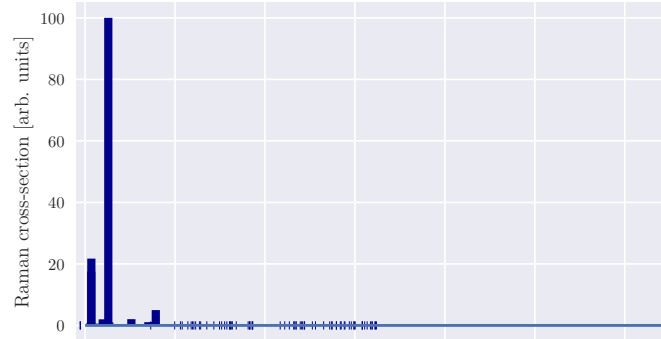
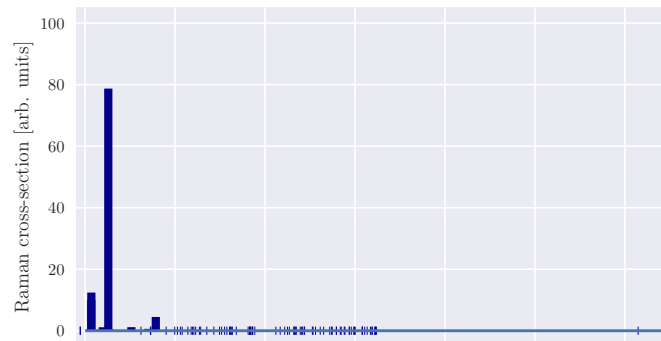
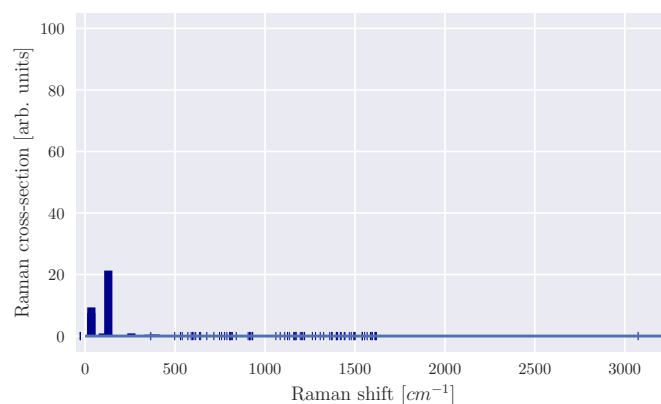
Computed 7-AGNR (3 units) ($\lambda_L = 532\text{nm}$) total Raman cross-section $\sigma'(\perp^s + \parallel^s)$ Computed 7-AGNR (3 units) ($\lambda_L = 532\text{nm}$) perpendicular Raman cross-section $\sigma'(\perp^s)$ Computed 7-AGNR (3 units) ($\lambda_L = 532\text{nm}$) parallel Raman cross-section $\sigma'(\parallel^s)$ 

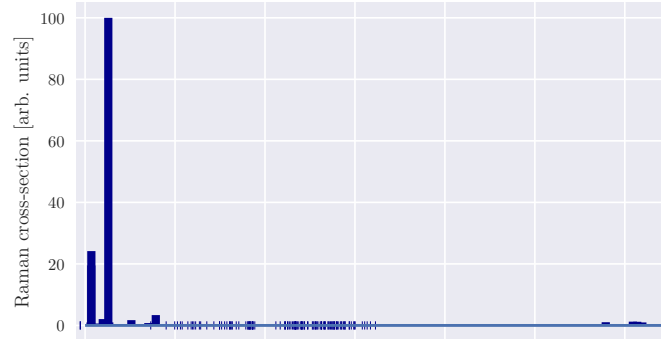
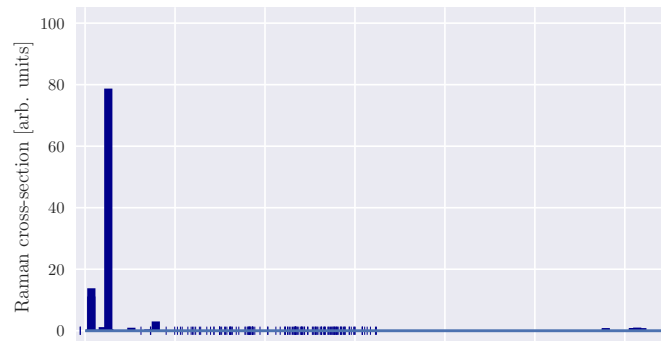
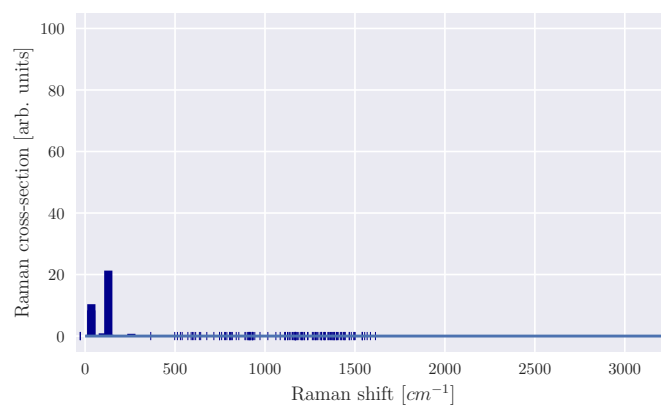
Computed 7-AGNR (3 units) ($\lambda_L = 785\text{nm}$) total Raman cross-section $\sigma'(\perp^s + \parallel^s)$ Computed 7-AGNR (3 units) ($\lambda_L = 785\text{nm}$) perpendicular Raman cross-section $\sigma'(\perp^s)$ Computed 7-AGNR (3 units) ($\lambda_L = 785\text{nm}$) parallel Raman cross-section $\sigma'(\parallel^s)$ 

7-AGNR (6 units)

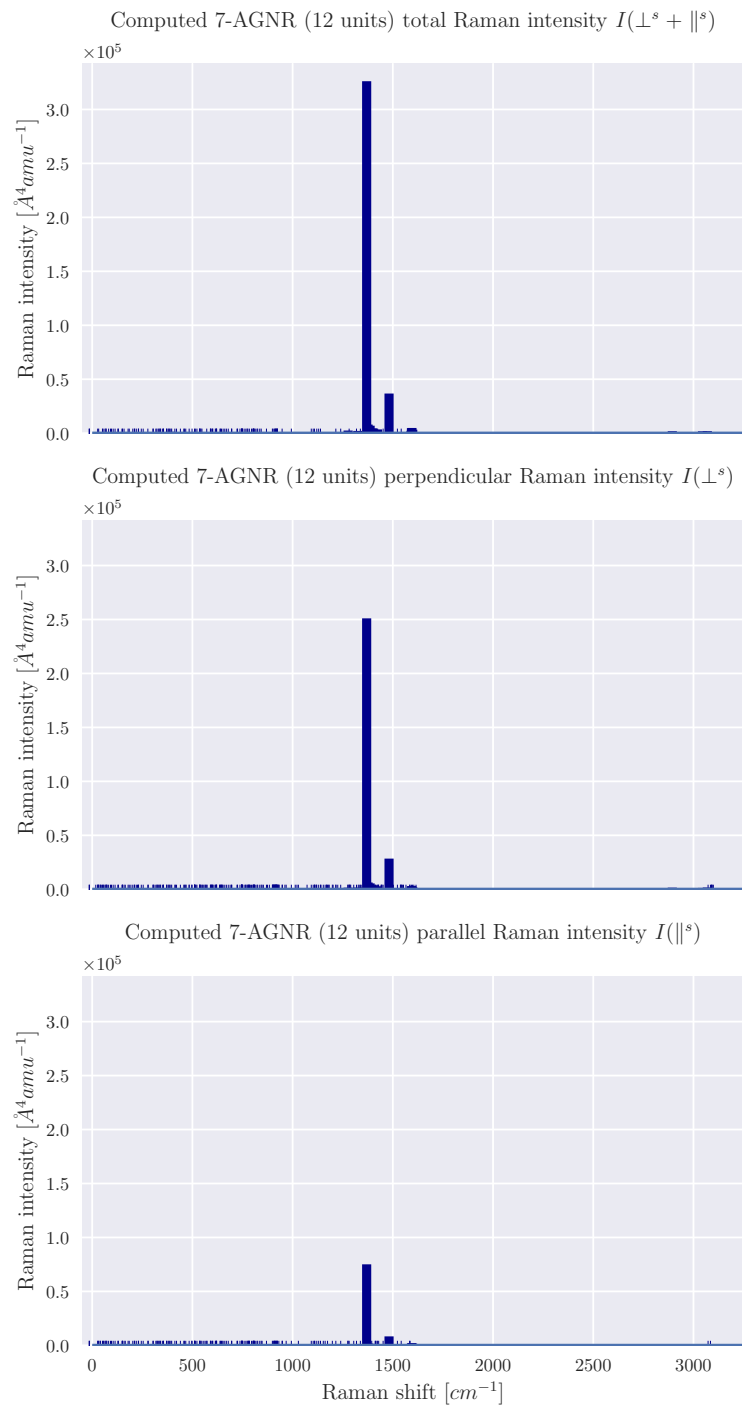


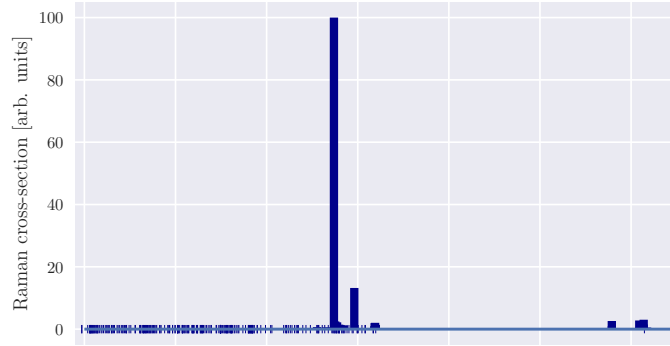
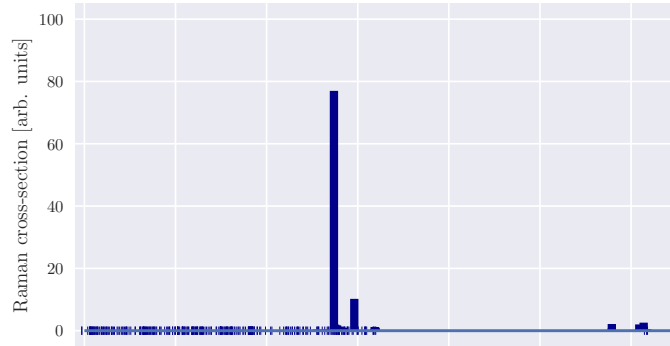
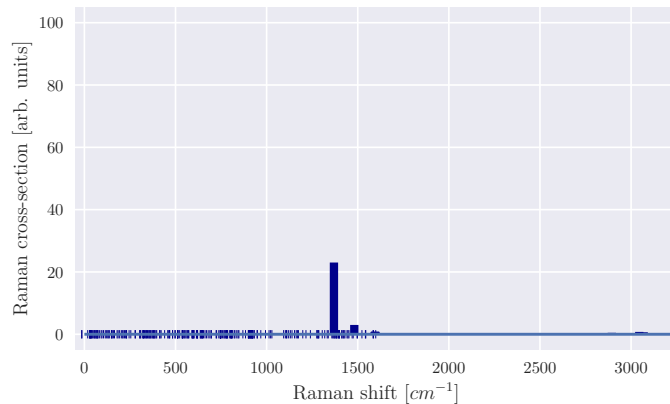
Computed 7-AGNR (6 units) ($\lambda_L = 0\text{nm}$) total Raman cross-section $\sigma'(\perp^s + \parallel^s)$ Computed 7-AGNR (6 units) ($\lambda_L = 0\text{nm}$) perpendicular Raman cross-section $\sigma'(\perp^s)$ Computed 7-AGNR (6 units) ($\lambda_L = 0\text{nm}$) parallel Raman cross-section $\sigma'(\parallel^s)$ 

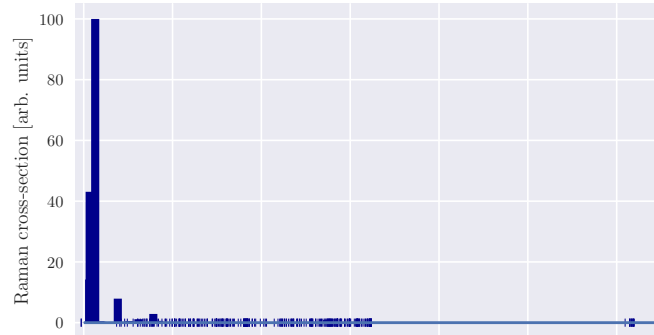
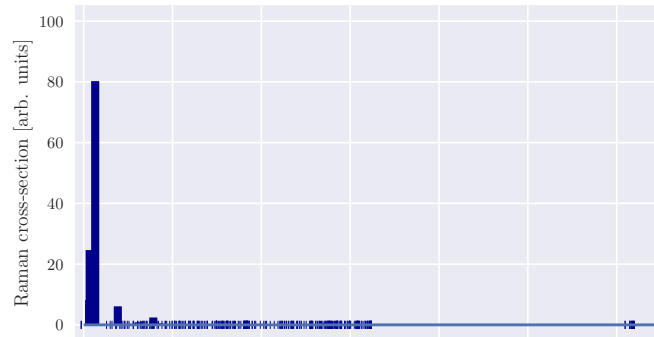
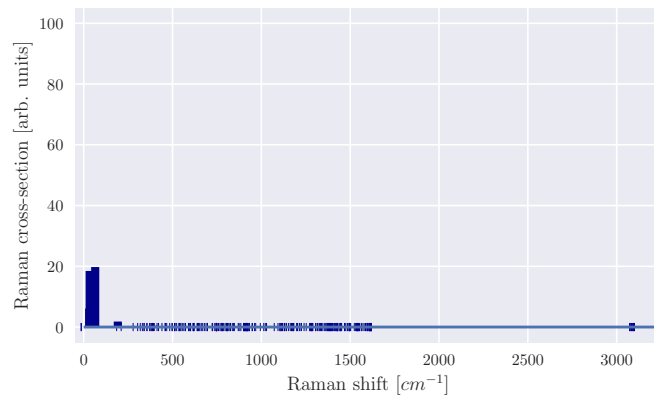
Computed 7-AGNR (6 units) ($\lambda_L = 532\text{nm}$) total Raman cross-section $\sigma'(\perp^s + \parallel^s)$ Computed 7-AGNR (6 units) ($\lambda_L = 532\text{nm}$) perpendicular Raman cross-section $\sigma'(\perp^s)$ Computed 7-AGNR (6 units) ($\lambda_L = 532\text{nm}$) parallel Raman cross-section $\sigma'(\parallel^s)$ 

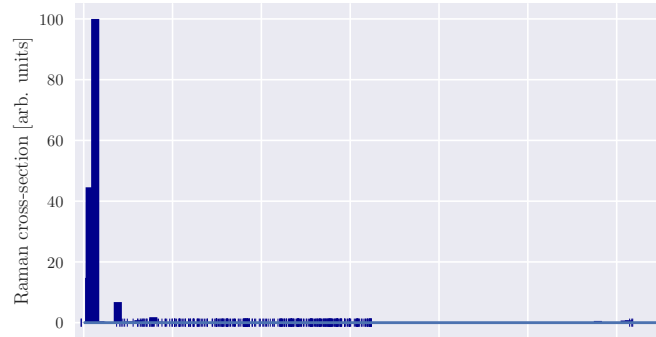
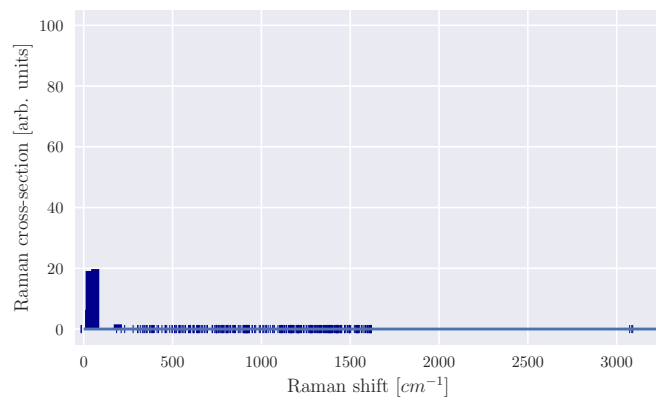
Computed 7-AGNR (6 units) ($\lambda_L = 785\text{nm}$) total Raman cross-section $\sigma'(\perp^s + \parallel^s)$ Computed 7-AGNR (6 units) ($\lambda_L = 785\text{nm}$) perpendicular Raman cross-section $\sigma'(\perp^s)$ Computed 7-AGNR (6 units) ($\lambda_L = 785\text{nm}$) parallel Raman cross-section $\sigma'(\parallel^s)$ 

7-AGNR (12 units)

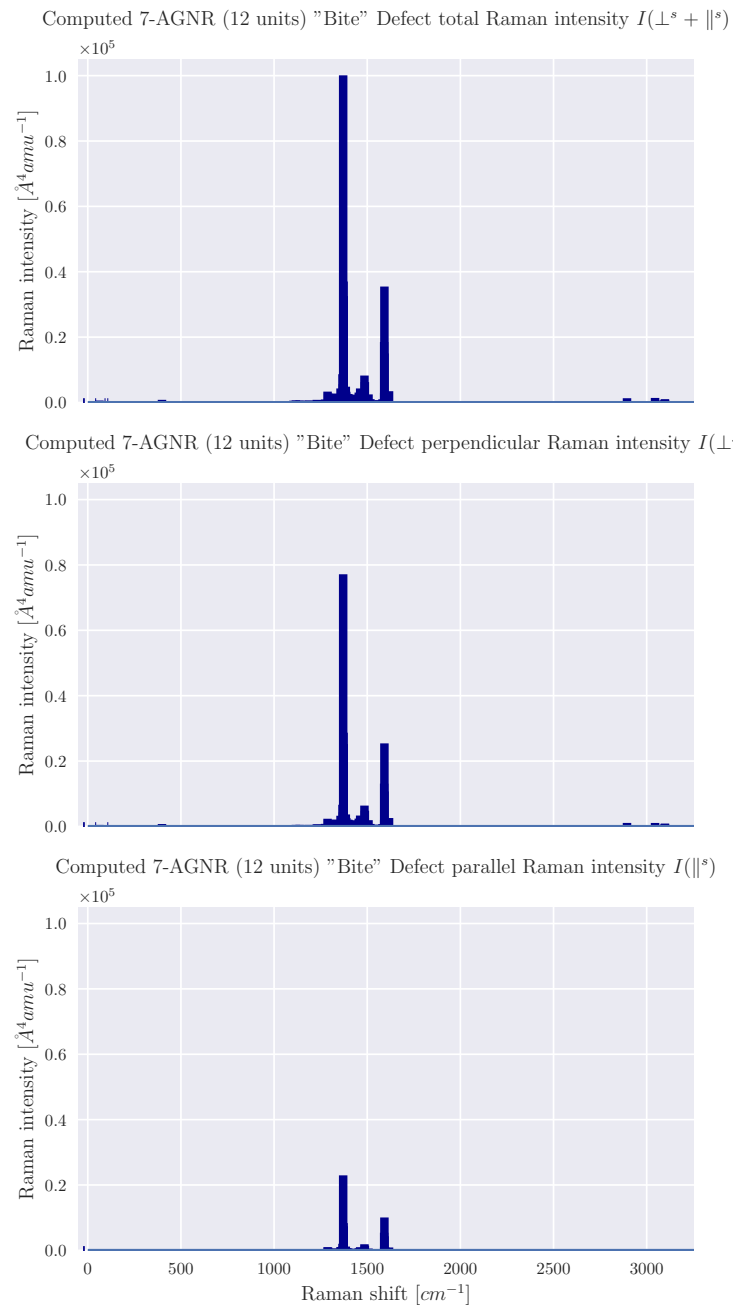


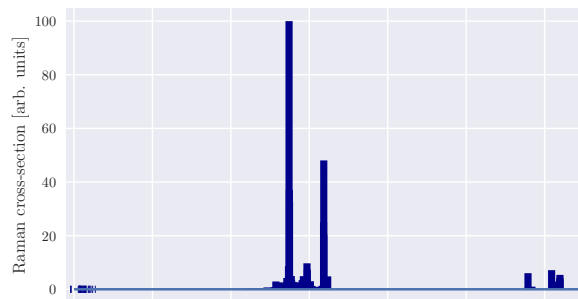
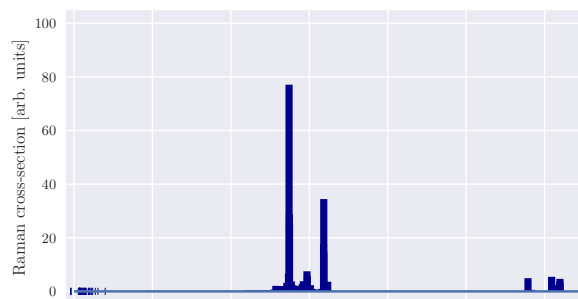
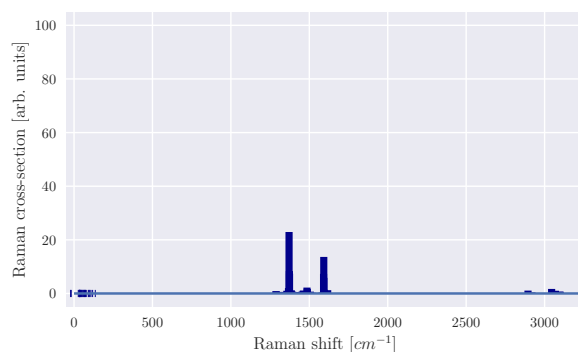
Computed 7-AGNR (12 units) ($\lambda_L = 0\text{nm}$) total Raman cross-section $\sigma'(\perp^s + \parallel^s)$ Computed 7-AGNR (12 units) ($\lambda_L = 0\text{nm}$) perpendicular Raman cross-section $\sigma'(\perp^s)$ Computed 7-AGNR (12 units) ($\lambda_L = 0\text{nm}$) parallel Raman cross-section $\sigma'(\parallel^s)$ 

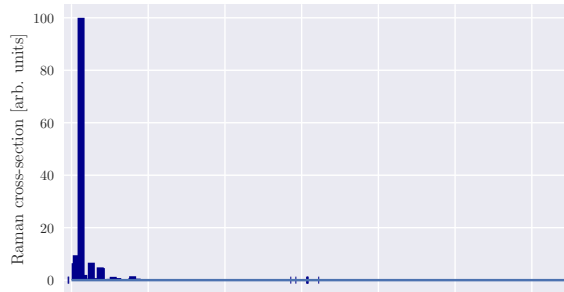
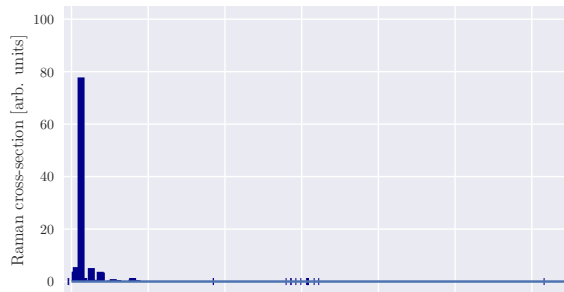
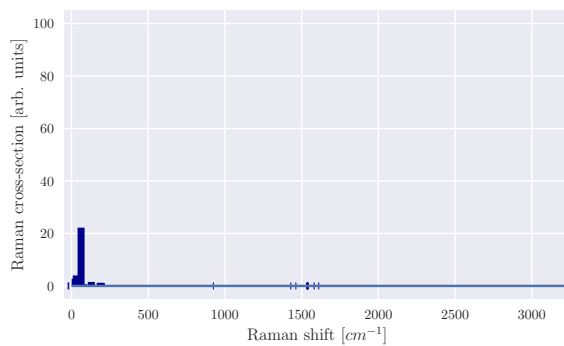
Computed 7-AGNR (12 units) ($\lambda_L = 532\text{nm}$) total Raman cross-section $\sigma'(\perp^s + \parallel^s)$ Computed 7-AGNR (12 units) ($\lambda_L = 532\text{nm}$) perpendicular Raman cross-section $\sigma'(\perp^s)$ Computed 7-AGNR (12 units) ($\lambda_L = 532\text{nm}$) parallel Raman cross-section $\sigma'(\parallel^s)$ 

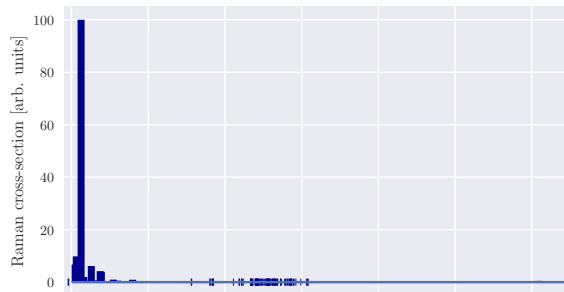
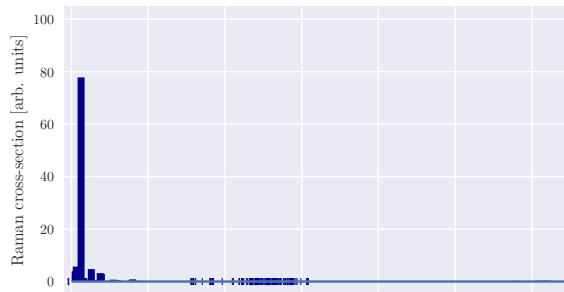
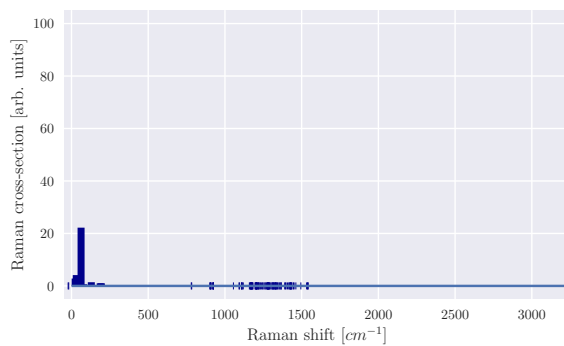
Computed 7-AGNR (12 units) ($\lambda_L = 785\text{nm}$) total Raman cross-section $\sigma'(\perp^s + \parallel^s)$ Computed 7-AGNR (12 units) ($\lambda_L = 785\text{nm}$) perpendicular Raman cross-section $\sigma'(\perp^s)$ Computed 7-AGNR (12 units) ($\lambda_L = 785\text{nm}$) parallel Raman cross-section $\sigma'(\parallel^s)$ 

7-AGNR (12 units): "Bite" defect

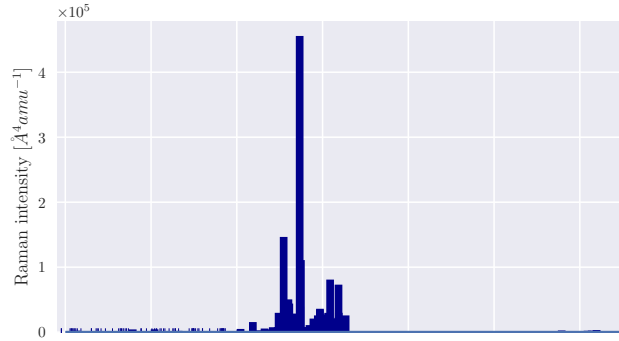
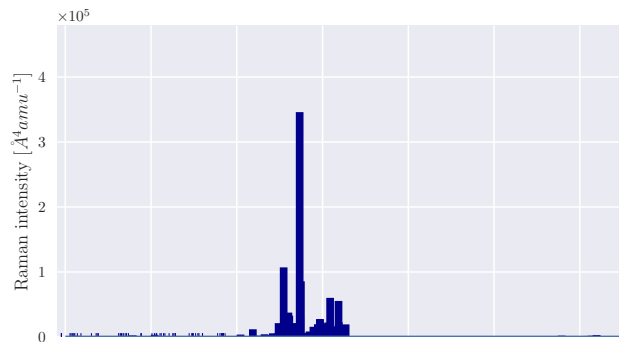
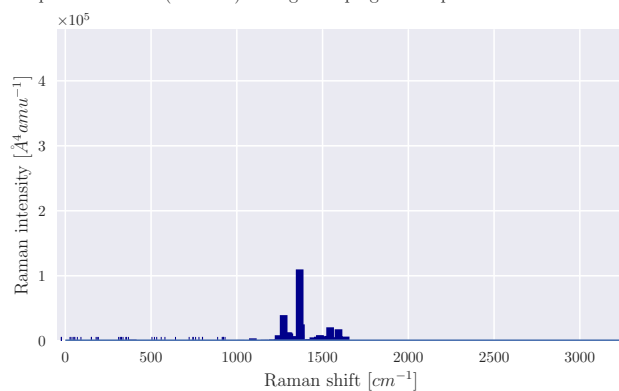


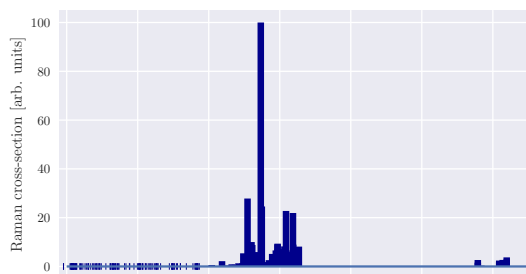
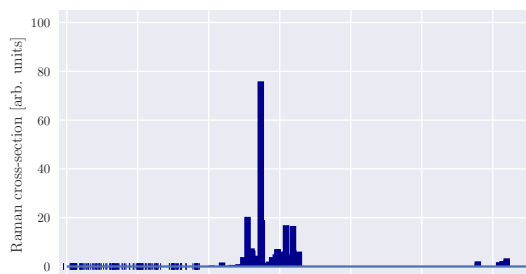
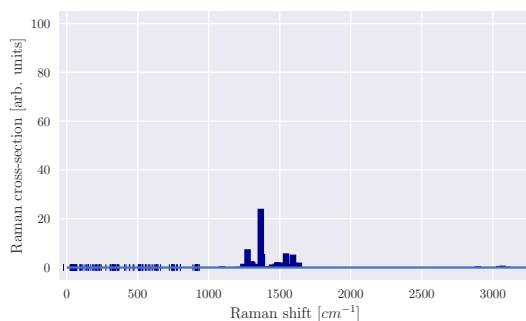
Computed 7-AGNR (12 units) "Bite" Defect ($\lambda_L = 0\text{nm}$) total Raman cross-section $\sigma'(\perp^s + \parallel^s)$ Computed 7-AGNR (12 units) "Bite" Defect ($\lambda_L = 0\text{nm}$) perpendicular Raman cross-section $\sigma'(\perp^s)$ Computed 7-AGNR (12 units) "Bite" Defect ($\lambda_L = 0\text{nm}$) parallel Raman cross-section $\sigma'(\parallel^s)$ 

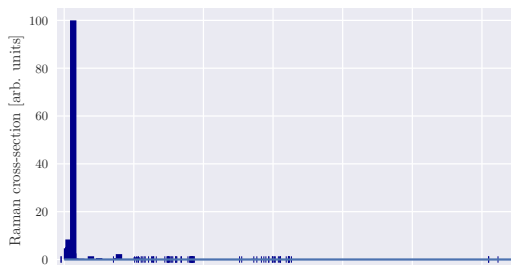
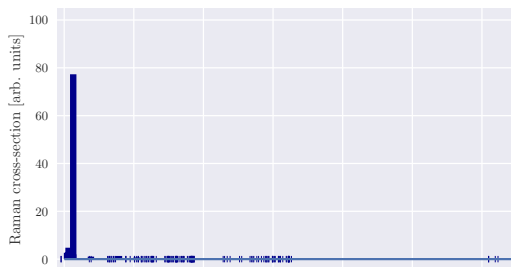
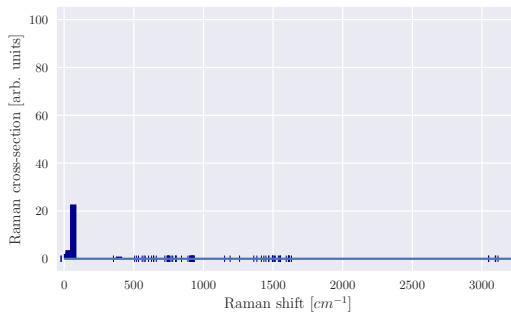
Computed 7-AGNR (12 units) "Bite" Defect ($\lambda_L = 532\text{nm}$) total Raman cross-section $\sigma'(\perp^s + \parallel^s)$ Computed 7-AGNR (12 units) "Bite" Defect ($\lambda_L = 532\text{nm}$) perpendicular Raman cross-section $\sigma'(\perp^s)$ Computed 7-AGNR (12 units) "Bite" Defect ($\lambda_L = 532\text{nm}$) parallel Raman cross-section $\sigma'(\parallel^s)$ 

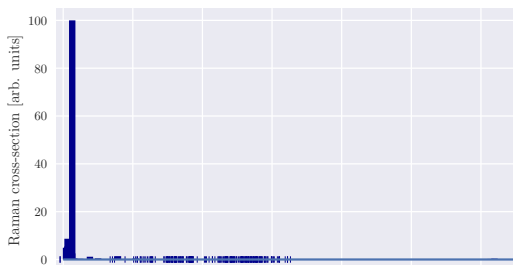
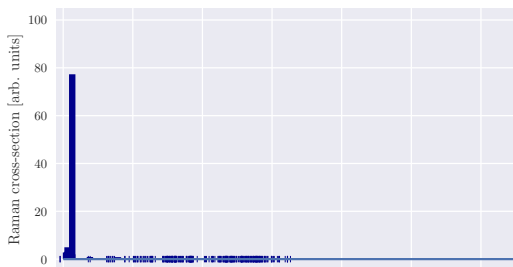
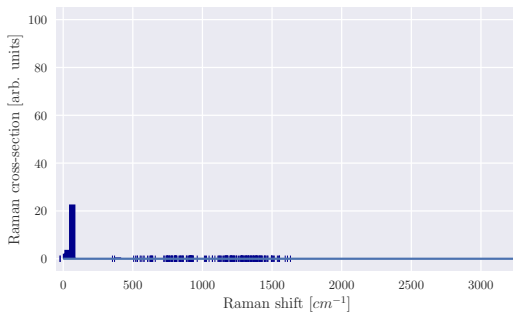
Computed 7-AGNR (12 units) "Bite" Defect ($\lambda_L = 785\text{nm}$) total Raman cross-section $\sigma'(\perp^s + \parallel^s)$ Computed 7-AGNR (12 units) "Bite" Defect ($\lambda_L = 785\text{nm}$) perpendicular Raman cross-section $\sigma'(\perp^s)$ Computed 7-AGNR (12 units) "Bite" Defect ($\lambda_L = 785\text{nm}$) parallel Raman cross-section $\sigma'(\parallel^s)$ 

7-AGNR (12 units): Nitrogen doping defect

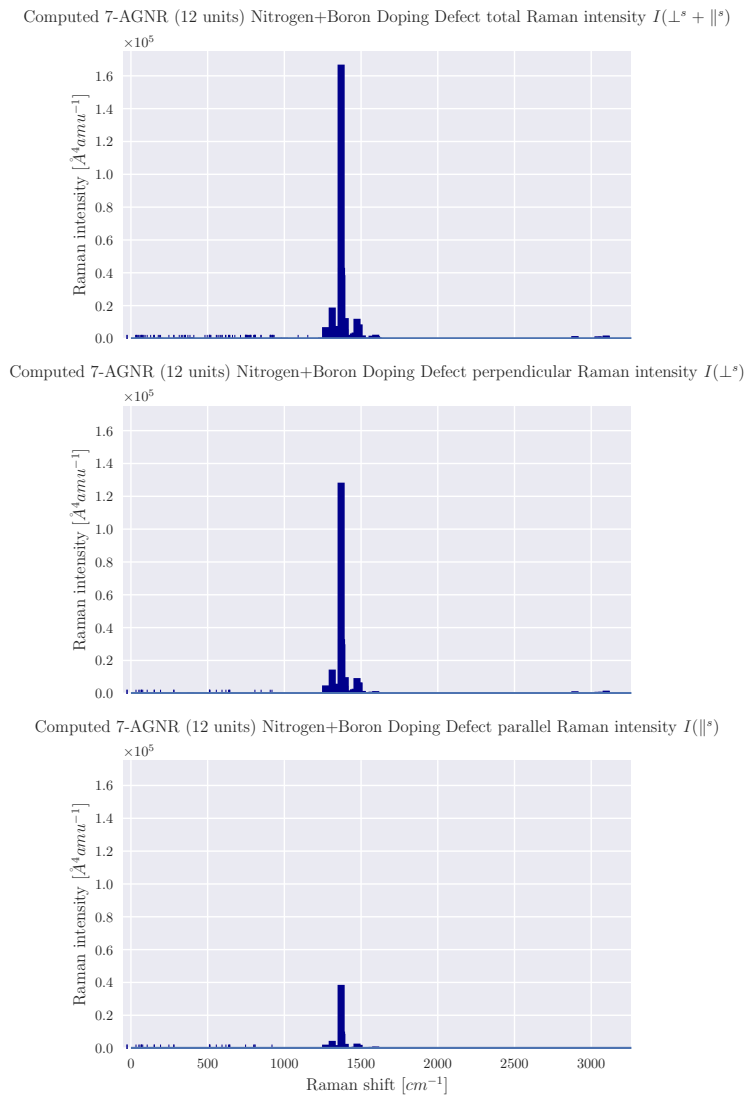
Computed 7-AGNR (12 units) Nitrogen Doping Defect total Raman intensity $I(\perp^s + \parallel^s)$ Computed 7-AGNR (12 units) Nitrogen Doping Defect perpendicular Raman intensity $I(\perp^s)$ Computed 7-AGNR (12 units) Nitrogen Doping Defect parallel Raman intensity $I(\parallel^s)$ 

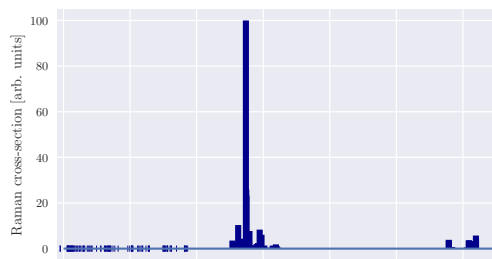
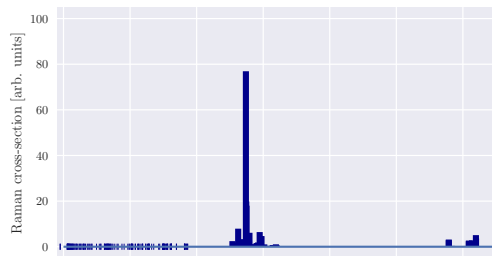
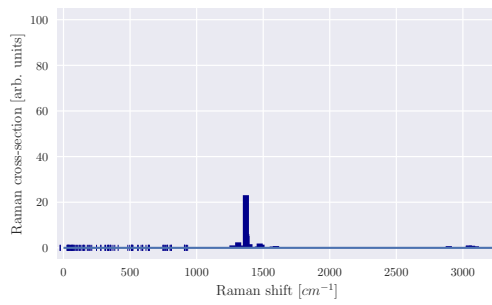
Computed 7-AGNR (12 units) Nitrogen Doping Defect ($\lambda_L = 0\text{nm}$) total Raman cross-section $\sigma'(\perp^s + \parallel^s)$ Computed 7-AGNR (12 units) Nitrogen Doping Defect ($\lambda_L = 0\text{nm}$) perpendicular Raman cross-section $\sigma'(\perp^s)$ Computed 7-AGNR (12 units) Nitrogen Doping Defect ($\lambda_L = 0\text{nm}$) parallel Raman cross-section $\sigma'(\parallel^s)$ 

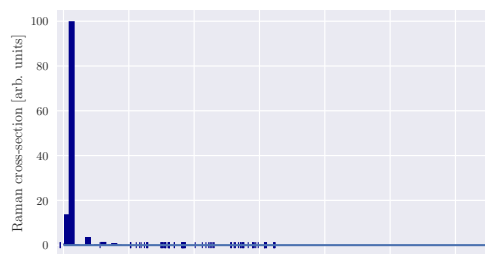
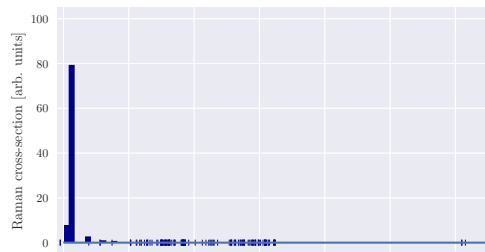
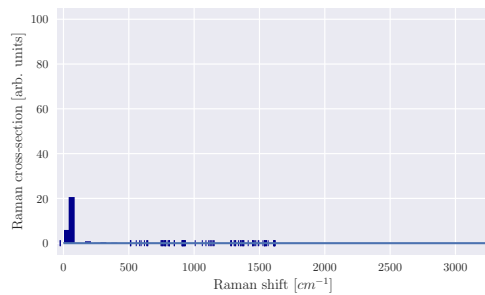
Computed 7-AGNR (12 units) Nitrogen Doping Defect ($\lambda_L = 532\text{nm}$) total Raman cross-section $\sigma'(\perp^s + \parallel^s)$ Computed 7-AGNR (12 units) Nitrogen Doping Defect ($\lambda_L = 532\text{nm}$) perpendicular Raman cross-section $\sigma'(\perp^s)$ Computed 7-AGNR (12 units) Nitrogen Doping Defect ($\lambda_L = 532\text{nm}$) parallel Raman cross-section $\sigma'(\parallel^s)$ 

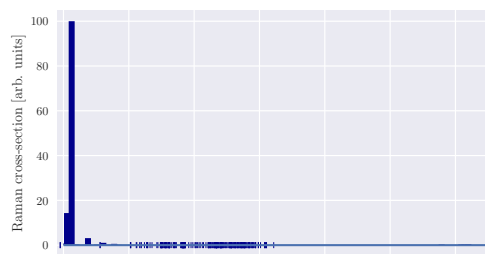
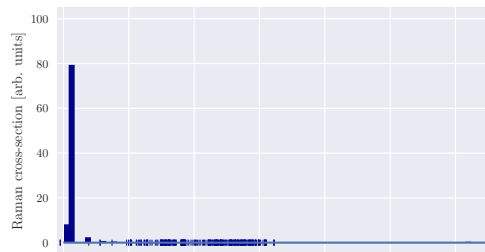
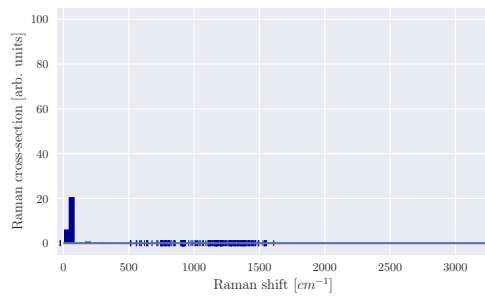
Computed 7-AGNR (12 units) Nitrogen Doping Defect ($\lambda_L = 785\text{nm}$) total Raman cross-section $\sigma'(\perp^s + \parallel^s)$ Computed 7-AGNR (12 units) Nitrogen Doping Defect ($\lambda_L = 785\text{nm}$) perpendicular Raman cross-section $\sigma'(\perp^s)$ Computed 7-AGNR (12 units) Nitrogen Doping Defect ($\lambda_L = 785\text{nm}$) parallel Raman cross-section $\sigma'(\parallel^s)$ 

7-AGNR (12 units): Nitrogen and boron doping defect



Computed 7-AGNR (12 units) Nitrogen+Boron Doping Defect ($\lambda_L = 0\text{nm}$) total Raman cross-section $\sigma'(\perp^s + \parallel^s)$ Computed 7-AGNR (12 units) Nitrogen+Boron Doping Defect ($\lambda_L = 0\text{nm}$) perpendicular Raman cross-section $\sigma'(\perp^s)$ Computed 7-AGNR (12 units) Nitrogen+Boron Doping Defect ($\lambda_L = 0\text{nm}$) parallel Raman cross-section $\sigma'(\parallel^s)$ 

Computed 7-AGNR (12 units) Nitrogen+Boron Doping Defect ($\lambda_L = 532\text{nm}$) total Raman cross-section $\sigma'(\perp^* + \parallel^*)$ Computed 7-AGNR (12 units) Nitrogen+Boron Doping Defect ($\lambda_L = 532\text{nm}$) perpendicular Raman cross-section $\sigma'(\perp^*)$ Computed 7-AGNR (12 units) Nitrogen+Boron Doping Defect ($\lambda_L = 532\text{nm}$) parallel Raman cross-section $\sigma'(\parallel^*)$ 

Computed 7-AGNR (12 units) Nitrogen+Boron Doping Defect ($\lambda_L = 785\text{nm}$) total Raman cross-section $\sigma'(\perp^s + \parallel^s)$ Computed 7-AGNR (12 units) Nitrogen+Boron Doping Defect ($\lambda_L = 785\text{nm}$) perpendicular Raman cross-section $\sigma'(\perp^s)$ Computed 7-AGNR (12 units) Nitrogen+Boron Doping Defect ($\lambda_L = 785\text{nm}$) parallel Raman cross-section $\sigma'(\parallel^s)$ 

Declaration of Originality

Declaration of Originality



Eidgenössische Technische Hochschule Zürich
Swiss Federal Institute of Technology Zurich

Declaration of originality

The signed declaration of originality is a component of every semester paper, Bachelor's thesis, Master's thesis and any other degree paper undertaken during the course of studies, including the respective electronic versions.

Lecturers may also require a declaration of originality for other written papers compiled for their courses.

I hereby confirm that I am the sole author of the written work here enclosed and that I have compiled it in my own words. Parts excepted are corrections of form and content by the supervisor.

Title of work (in block letters):

SIMULATING RAMAN SPECTRA:
A CP2K-BASED IMPLEMENTATION AND ITS APPLICATION TO
DEFECTIVE GRAPHENE NANORIBBONS

Authored by (in block letters):

For papers written by groups the names of all authors are required.

Name(s):

HUBMANS

First name(s):

BERT PETER

With my signature I confirm that

- I have committed none of the forms of plagiarism described in the '[Citation etiquette](#)' information sheet.
- I have documented all methods, data and processes truthfully.
- I have not manipulated any data.
- I have mentioned all persons who were significant facilitators of the work.

I am aware that the work may be screened electronically for plagiarism.

Place, date

Zürich, 31/08/2020

Signature(s)

For papers written by groups the names of all authors are required. Their signatures collectively guarantee the entire content of the written paper.